Repeatability-dependent detection thresholds for time-lapse seismic CO_2 monitoring

Moses Falowo

Jackson School of Geosciences, The University of Texas at Austin, Austin, Texas, USA

ORCID: https://orcid.org/0009-0009-6744-7409
Email: falowomoses@gmail.com

This manuscript is a non-peer-reviewed preprint submitted to EarthArXiv.

Keywords: time-lapse seismic; CO_2 storage monitoring; detectability; repeatability; NRMS; rock physics; signal detection; Sleipner

This PDF contains the full paper followed by the complete supplementary material (Figures S1–S10).

Repeatability-dependent detection thresholds for time-lapse seismic CO_2 monitoring

Moses Falowo

Jackson School of Geosciences, The University of Texas at Austin, Austin, Texas, USA. falowomoses@gmail.com

Abstract

We quantify the smallest CO_2 layer that a time-lapse seismic survey pair can detect as a function of repeatability, measured by the normalized root-mean-square (NRMS) difference, in a controlled, Sleipner-like synthetic study. Gassmann fluid substitution under four fluid-mixing treatments feeds one-dimensional layer models, checked against two-dimensional finite-difference gathers, and calibrated nonrepeatability sets NRMS from 10% to 60%. Detection is a hypothesis test at a false-alarm probability of 0.05, with 1200 null realizations for each frequency and noise level and 40 held-out signal realizations in each of 1728 cells, for four detectors: windowed energy, a clean-template matched filter, a generic-template filter, and a small convolutional neural network (CNN). At 30 Hz, a CO_2 saturation of 0.8, and uniform (Reuss) mixing, the energy detector's minimum detectable thickness rises from the 1-m grid floor at NRMS 10% to 4.5 m at NRMS 60%, and Voigt mixing roughly doubles the latter. The energy detector's minimum detectable free-phase mass per area rises over the same NRMS range from 25 (a censored grid corner) to 253 kg/m^2, both at the lowest saturation tested. At 30 and 45 Hz and NRMS of 40% and above, the energy detector and the CNN increasingly exceed the matched filter's area under the receiver operating characteristic curve, consistent with nonrepeatability misaligning the signal; at 15 Hz the matched filter keeps its advantage. At fixed NRMS, in-window reflectivity and host stiffness also move the 30-Hz energy-detector threshold, and a consolidated host suppresses detection. Predictions agree with 11 published Sleipner observables within a factor of 1.41, a consistency check rather than validation. Published Sleipner NRMS of 45%–53% lies near the 50% grid level, where energy-detector, matched-filter, and CNN thresholds span 1.8–3.0 m. A credible detection claim therefore states the repeatability, the false-alarm probability, and the detector together.

Introduction

Geologic CO_2 storage must demonstrate containment and conformance over decades, and time-lapse (4D) seismic surveying is the main measurement for both (Jenkins et al., 2015; Furre et al., 2017). The smallest change in stored CO_2 that a survey pair can detect sets the survey repeat interval and investment and decides whether a monitoring plan is credible (Harvey et al., 2022). That limit depends on survey repeatability, summarized by the normalized root-mean-square (NRMS) difference (Kragh and Christie, 2002): the root-mean-square (rms) amplitude of the difference between two traces, as a percentage of their average rms amplitude.

Field programs report detectability empirically, one site at a time. At Sleipner, repeated surveys have imaged the growing plume in the Utsira Sand (Arts et al., 2004; Chadwick et al., 2010; Furre et al., 2017), and Chadwick et al. (2014) reported that layers thicker than about 2 m are readily detectable, whereas layers thinner than about 0.5 m are difficult. White et al. (2013) tested the limits of time-lapse resolution for thin

layers in the same plume, and Ghaderi and Landrø (2009) combined amplitude and time-shift analysis of prestack time-lapse data to estimate the thickness and velocity change of its CO_2 layers. At the Aquistore land site, preinjection surveys measured the repeatability of a sparse permanent array and asked what CO_2 signal would exceed it (Roach et al., 2015; White et al., 2015), postinjection imaging tracked the plume (Roach and White, 2018), and Park et al. (2024) trained a learned detector on preinjection surveys alone to identify the plume in later ones. At a field research station, vertical seismic profiling detected small controlled CO_2 injections (Kolkman-Quinn et al., 2023). These programs build on 4D feasibility screening (Lumley et al., 1997), quantitative time-lapse analysis (Landrø, 2001), and monitoring-scale mass estimation (Ivanova et al., 2012), reviewed for CO_2 storage by Lumley (2010). Each estimate refers to one site, one realized noise state, and one, usually implicit, detection criterion.

Synthetic studies can control the noise level, the scenario, and the detection criterion, but each published study fixes at least one of them. Roach et al. (2017) forward-modeled the Aquistore reservoir to ask when injected CO_2 exceeds the site's measured noise floor, and Wang et al. (2018) simulated leakage scenarios at a model storage site and derived NRMS-based detection thresholds and earliest detection times. To our knowledge, no published study reports minimum detectable thickness as a continuous function of NRMS at a controlled false-alarm probability, across detectors of known statistical standing, with Monte Carlo uncertainty against exact ground truth.

We build that function from a seeded synthetic chain in which NRMS is an experimental axis: Gassmann rock physics under four fluid-mixing treatments, one-dimensional layer models checked against two-dimensional finite-difference gathers, calibrated nonrepeatability from 10% to 60% NRMS, and binary hypothesis tests against empirical null distributions at a fixed false-alarm probability. Four detectors span the range of signal knowledge: a windowed energy detector, a generic-template filter, a small convolutional neural network (CNN), and a matched filter that correlates the difference with the exact noise-free response of each cell, which would be the Neyman–Pearson detector for a known signal if the noise were additive, white, and Gaussian (Kay, 1998).

The result is a threshold chart that a monitoring designer can read at a survey pair's measured NRMS, dominant frequency, and chosen false-alarm probability. The modeling is acoustic and uses synthetic stationary noise, detection is a single-trace test in a known window, and the comparison with published Sleipner observations is a consistency check, not field validation.

Methods

Study design and detection criterion

A dense Monte Carlo grid of one-dimensional (1D) layer models carries the detection statistics, and a two-dimensional (2D) finite-difference subset tests their transfer (Figure 1). Noise-free signals are synthesized once per cell, and all variability is added in the data domain. A cell is one combination of layer thickness h, CO_2 saturation S_{CO_2}, dominant (spectral-peak) frequency f_d of the wavelet (equation 3), and target NRMS; an ensemble is all cells at one f_d and NRMS level.

A layer counts as detected when the probability of detection P_D reaches 0.9 at false-alarm probability $P_{FA} = 0.05$, with $P_{FA} = 0.01$ as the stricter case. Detection is a single-trace test, in a known window, of

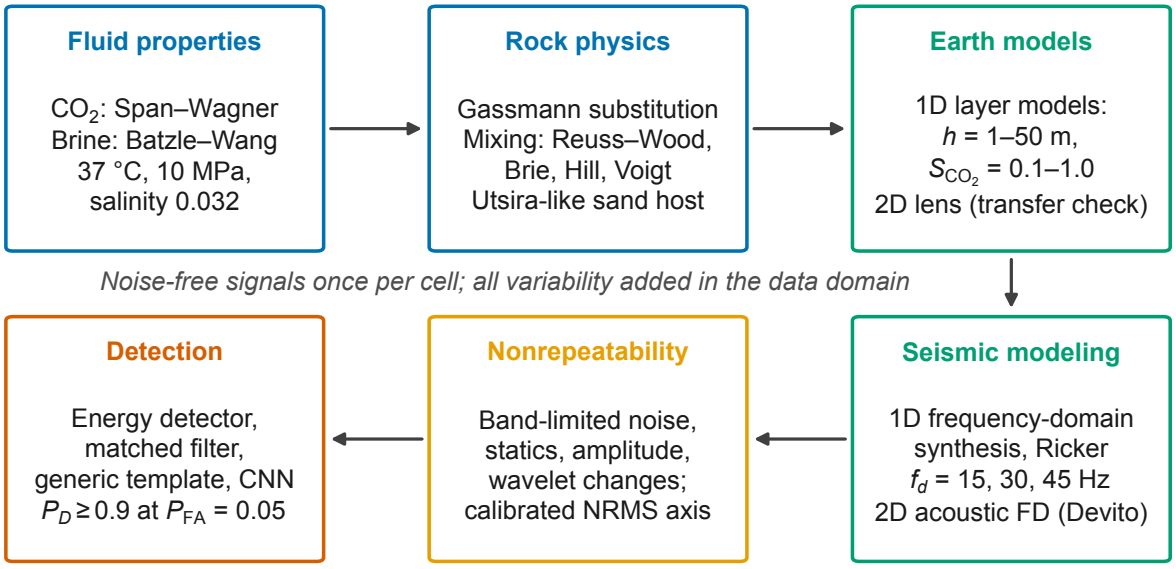


Figure 1. Study workflow. Fluid properties feed Gassmann rock physics with four mixing treatments; 1D and 2D models give noise-free signals; calibrated noise sets the NRMS axis; four detectors give detection probability at a fixed false-alarm probability. FD, finite difference; salinity is a weight fraction.

the null hypothesis H_0, no CO_2 change, against H_1, a change present, with thresholds set on null realizations and a per-trace, per-window false-alarm rate. The minimum detectable thickness $h_{\min}$ is the first up-crossing of the target with increasing thickness at $S_{CO_2} = 0.8$ in each ensemble, interpolated linearly and censored at the 1-m grid floor and the 50-m grid maximum; because P_D need not rise monotonically with thickness, this is the thinnest crossing. The minimum detectable mass per area is the smallest grid-cell m_A (equation 8) among cells that meet the target, without interpolation. Unless stated otherwise, thresholds refer to 30 Hz, $S_{CO_2} = 0.8$, and $P_{FA} = 0.05$, the default operating point.

Fluid properties

CO_2 properties come from the Span–Wagner equation of state (Span and Wagner, 1996) in CoolProp (Bell et al., 2014), with the adiabatic bulk modulus equal to density times the squared sound speed, and gas-free brine follows Batzle and Wang (1992). The reference conditions are 37 °C, 10 MPa, and a salinity of 0.032 weight fraction, the value Audigane et al. (2007) assumed for the Utsira porewater, consistent with Portier and Rochelle (2005). The CO_2 is then supercritical and about 40 times more compressible than the brine it replaces, with density $\rho_{CO_2} = 683.4$ kg/m^3 and bulk modulus $K_{CO_2} = 0.0637$ GPa, against brine values $\rho_{\text{brine}} = 1018.8$ kg/m^3 and $K_{\text{brine}} = 2.518$ GPa. A 41 × 51 grid over 5–25 MPa and 30–80 °C maps the fluid properties (Figure S1), but all detection runs use the reference condition.

Rock physics

Gassmann fluid substitution (Gassmann, 1951) gives the saturated bulk modulus,

$$K_{\text{sat}} = K_{\text{dry}} + \frac{\left(1 - K_{\text{dry}}/K_s\right)^2}{\phi/K_{\text{fl}} + (1-\phi)/K_s - K_{\text{dry}}/K_s^2}, \tag{1}$$

where K_{dry}, K_s, and K_{fl} are the drained-frame, mineral, and pore-fluid bulk moduli and ϕ the porosity; the shear modulus G does not depend on the fluid. Equation 1 assumes an isotropic, monomineralic frame in the low-frequency limit, with no fluid–frame chemistry. Four mixing treatments set K_{fl} at partial saturation: Reuss–Wood averaging (Wood, 1955), the primary uniform-mixing case; Voigt averaging, the conventional patchy-saturation shortcut used in place of the Gassmann–Hill end member (Mavko et al., 2009); the empirical Brie law (Brie et al., 1995) with exponent $e = 3$; and the Hill average (Mavko et al., 2009), the arithmetic mean of the Reuss and Voigt values, an ad hoc midpoint. The Brie curve crosses below Reuss between $S_{\text{CO}_2} = 0.82$ and 0.83, so it carries no bound guarantee.

The primary host is an unconsolidated Utsira-like sand (Dupuy et al., 2017) with porosity 0.37, grain density 2664 kg/m^3, and dry-frame, shear, and mineral moduli of 2.56, 0.84, and 39.29 GPa. A brine-saturated consolidated sandstone, representative of the velocity–porosity trends of Han (1986), is the deep reference unit of every 1D and 2D model and an alternative host in the sensitivity analysis; it has porosity 0.20, dry-frame and shear moduli of 14.00 and 12.00 GPa, and quartz grains of 36.60 GPa and 2650 kg/m^3 (Mavko et al., 2009). A soft sand (Carcione et al., 2006), used only in the sensitivity analysis, has porosity 0.36, grain density 2600 kg/m^3, and dry-frame, shear, and mineral moduli of 1.37, 0.82, and 40.00 GPa. The brine-saturated Utsira-like sand has P-velocity $V_P = 2104$ m/s and density 2055 kg/m^3, within 3% of the logs of Williams and Chadwick (2012); Figure 2 shows the saturation response of both sands.

Earth models, wavelet, and conventions

The 1D model is homogeneous brine-saturated Utsira-like sand from the surface down, with no water layer or overburden reflector. A CO_2 layer occupies depths z from 850 m to 850 m + h, and brine sand continues below it to the deep unit at 1150 m. The baseline holds only the deep reflection; the monitor adds the layer's top and base reflections and delays the deep one, with primaries only, without multiples or transmission loss. The 2D model places a lens with a flat top at 850 m and a parabolic base in a 4000 m × 1500 m section, with thickness profile

$$H(x) = h \max\left[0,\ 1 - \left(\frac{x - x_0}{L}\right)^2\right], \tag{2}$$

where h is the lens thickness at its center, x horizontal position, x_0 the domain center, and $L = 500$ m the half-width, with uniform saturation in the lens.

The source wavelet is a Ricker wavelet,

$$w(t) = \left(1 - 2\pi^2 f_d^2 t^2\right) \exp\left(-\pi^2 f_d^2 t^2\right), \tag{3}$$

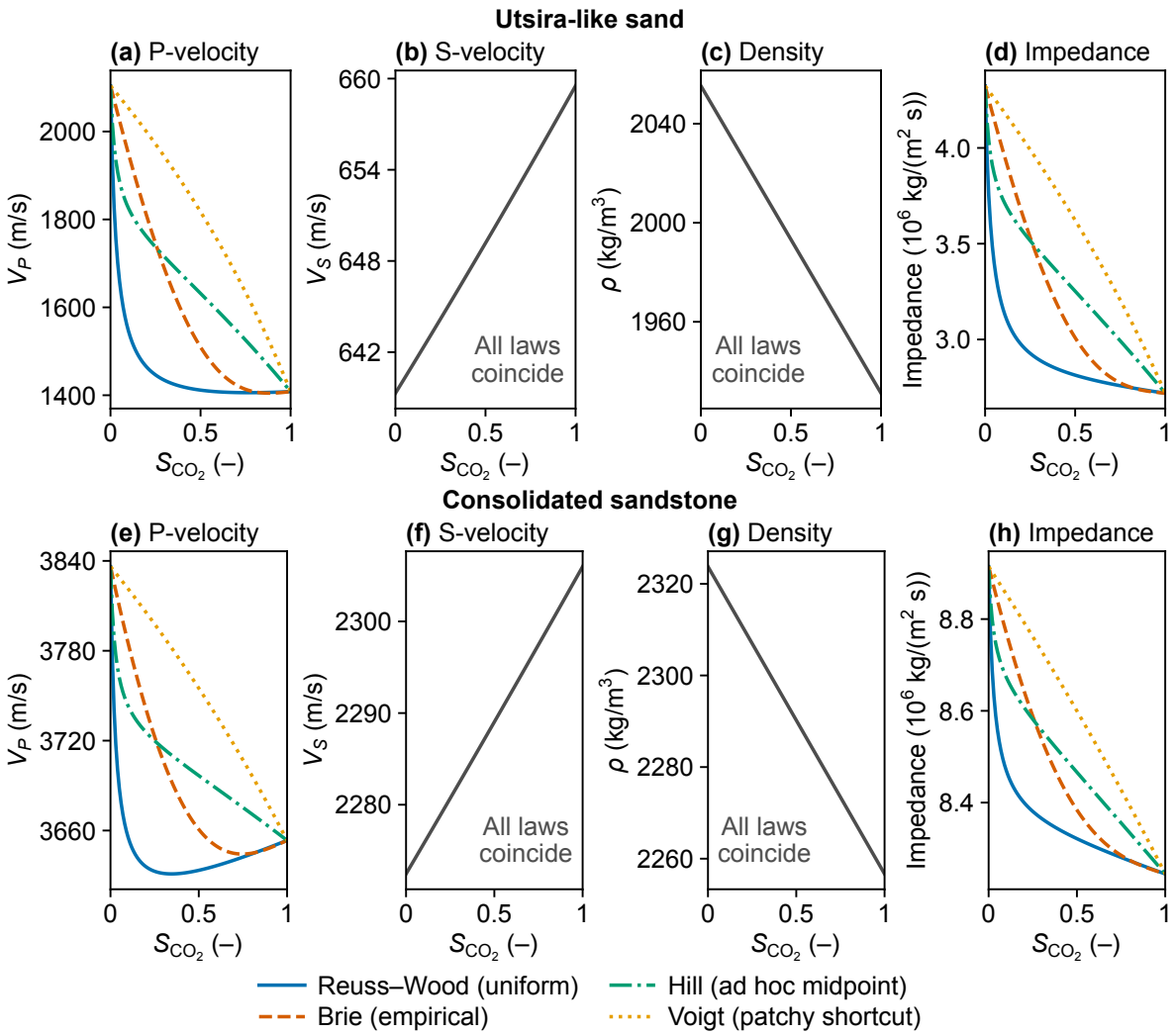


Figure 2. (a–d) P-velocity, S-velocity, density, and acoustic impedance versus CO_2 saturation for the four fluid-mixing treatments in the Utsira-like sand; (e–h) the same for the consolidated sandstone, which changes far less.

with time t and f_d = 15, 30, and 45 Hz. Polarity follows the SEG positive standard (Sheriff, 2002): an increase in acoustic impedance gives a positive amplitude. Traces are sampled at 0.5 ms, with 1600 samples from t = 0.5 s.

Every trace also carries Ricker-band-limited white background reflectivity, one draw per frequency, whose rms in the reservoir interval (the detection window defined below) is 0.5 of the rms of the background-free deep event. The background is identical in baseline, monitor, null, and CNN traces, so it cancels in noise-free differences, but nonrepeatability acting on it places null energy inside the window. Sleipner data do not constrain its level.

One-dimensional synthesis, tuning, and push-down

The 1D traces are synthesized exactly in the frequency domain, as the analytic Ricker spectrum times one subsample phase ramp per reflector weighted by its reflection coefficient, which keeps reflector times

free of sampling error. For the opposite-polarity reflection pair of a thin layer (Widess, 1973), the criterion of Kallweit and Wood (1982) places tuning at the peak-to-trough time, $T_{pt} = \sqrt{6}/(2\pi f_d)$ for a Ricker wavelet, so the tuning thickness is $vT_{pt}/2$ for layer P-velocity v, and the quarter-wavelength rule, with wavelength $\lambda = v/f_d$, overpredicts it by $\pi/\sqrt{6} \approx 1.283$. Tuning thickness is measured as the parabola-refined peak of the windowed maximum absolute amplitude over a fine thickness sweep. Push-down is measured, on a sweep sampled more finely than the detection grid, by crosscorrelation around the deep event, with parabolic subsample refinement, and compared with $\Delta t = 2h\,(1/v_{\mathrm{CO_2}} - 1/v_{\mathrm{brine}})$, where $v_{\mathrm{CO_2}}$ and v_{brine} are the P-velocities of CO_2-bearing and brine sand.

Two-dimensional variable-density acoustic modeling

Devito (Louboutin et al., 2019; Luporini et al., 2020) solves

$$\frac{1}{\rho v^2}\frac{\partial^2 p}{\partial t^2} + \eta\,\frac{\partial p}{\partial t} = \nabla\cdot\left(\frac{1}{\rho}\nabla p\right), \tag{4}$$

where p is pressure, ρ density, v P-velocity, and η a damping coefficient, nonzero only in absorbing layers on all sides, with no free surface. The pressure-only scheme is second order in time, and its variable-density operator uses half-cell-staggered first derivatives of order 8. Acoustic modeling captures the near-normal-incidence reflectivity change that the zero-offset detectors use. The 2.5-m grid samples the slowest cell of the baseline model at 11.2 points per minimum wavelength and the slower CO_2 layer of the monitor at 7.5, above the minimum of 5 that the modeling code enforces, and the 0.3382 ms time step equals Devito's critical step (ratio 1.000), which lies below the stability limit of this staggered scheme. One shot at $f_d = 30$ Hz is fired at 10 m depth above the lens center ($x = 2000$ m), and the unmigrated common-shot gathers are resampled to 0.5 ms. A line of 361 receivers at 10 m depth, spaced 10 m, runs from $x = 200$ to 3800 m. Lens thickness is quantized to the 2.5-m cell, so the nominal 1-m and 2-m lenses are identical in 2D. On coarser test grids, direct-arrival times match analytic values within 1%, flat-reflector times within 1%, the reflection has positive polarity, and the boundary residual stays below 2% of the direct-arrival peak.

Noise and nonrepeatability

Five perturbations model nonrepeatability, with magnitudes listed for a unit mix, the reference composition that a single master scale later multiplies. Additive Gaussian noise, band-limited to 6–80 Hz with tapered edges, is drawn independently for each survey at 3% of a reference rms amplitude, the rms of the baseline deep reflection in the NRMS window. Each monitor trace receives a static shift with standard deviation 0.5 ms, applied as a subsample Fourier phase ramp, and an amplitude scalar with standard deviation 3%. The wavelet changes survey-wide by a dominant-frequency change of 2% and a phase rotation of 3°, with signs drawn per realization. These four act on the monitor only, as the relative perturbation between the two surveys. Source and receiver mispositioning, which would require remodeling, is excluded.

Repeatability is measured by the normalized rms difference of Kragh and Christie (2002),

$$\mathrm{NRMS} = 200 \times \frac{\mathrm{rms}(a-b)}{\mathrm{rms}(a)+\mathrm{rms}(b)}, \tag{5}$$

where a and b are the baseline and monitor traces, in a window of ±100 ms centered on the deep reflector of the background-bearing baseline, outside the detection window (shortened for the consolidated host so that it stays outside). It is reported as the trace-pair median; NRMS pooled over a whole section runs higher at identical physics.

The master scale, one per frequency and NRMS level, ranges from 0.75 to 7.125 over the grid, so at high NRMS the operating perturbations are several times the listed values. The scale is set by bisection on the median NRMS of a fixed-seed null ensemble, whose medians land within 1.0 NRMS point of target; the production nulls, drawn from separate seeds, deviate more at high NRMS (Results).

Detectors

Let d be the noisy monitor minus the noisy baseline in the detection window W of N_W samples, and s the noise-free difference in W. The window opens $1.2/f_d$, or 1.2 dominant periods, before the baseline top reflection and closes the same interval after the top time plus 75 ms, an allowance that covers the latest base arrival on the grid. It excludes the deep reflector, so no detector uses push-down. The energy detector, the statistical form of a windowed rms difference-amplitude map, is

$$\Lambda_E = \left(\frac{1}{N_W} \sum_{i \in W} d_i^2 \right)^{1/2}, \tag{6}$$

and the matched filter,

$$\Lambda_M = \frac{\langle d, s \rangle}{\|s\|}, \tag{7}$$

correlates the data with the exact noise-free signature of the cell, an oracle template and an idealized form of correlation with a forward-modeled type response. This zero-lag, signed, unwhitened statistic is the Neyman–Pearson detector only for a known signal in additive white Gaussian noise (Kay, 1998). The additive noise here is band-limited, so the statistic is not optimal even without nonrepeatability. The generic-template filter ("mismatched" in figure legends) computes Λ_G with the unit-norm clean signature of the $h = 20$ m, $S_{CO_2} = 0.8$ cell at the same frequency in place of s, as an interpreter applying one type model everywhere would; being signed, it can give an area under the receiver operating characteristic curve (AUC) below one half.

The CNN has 23361 parameters in three convolutional blocks of 16, 32, and 64 channels with kernels of 9 samples and rectified linear activations, max pooling by a factor of 2 after the first two, global average pooling, and a linear head whose output logit is the statistic Λ_C. One network per ensemble and seed is trained on the training signal realizations of all cells plus an equal-size null stream and validated on the validation realizations plus a second such stream, both streams disjoint from the threshold nulls. Training uses binary cross-entropy and the Adam optimizer, in mini-batches of 256 examples at a learning rate of 0.001, until 5 epochs pass without improvement in validation AUC (Figure S2); inputs are divided by the median rms of the training nulls.

Monte Carlo design, thresholds, and mass proxy

The grid crosses 16 thicknesses (1 to 8 m in 1-m steps, then 10, 12, 15, 20, 25, 30, 40, and 50 m), 6 saturations (0.1, 0.2, 0.4, 0.6, 0.8, and 1.0), 3 frequencies, and 6 NRMS levels from 10% to 60%, giving 1728 cells per detector. Each cell carries 150 signal realizations, and each ensemble shares 1200 null realizations. For comparability with the CNN, the last 40 signal realizations form the held-out test split for all detectors, and the other 90 and 20 train and validate the CNN for at most 30 epochs, with 3 seeds that vary only initialization and batch order. The threshold γ is the empirical $(1 - P_{\mathrm{FA}})$ quantile of the nulls at the next-higher order statistic, and detection requires a statistic strictly above γ, so in-sample false alarms never exceed P_{FA}; at $P_{\mathrm{FA}} = 0.01$ the thresholds rest on 12 expected false alarms. The matched statistic is recomputed per cell on the shared nulls. Detection probability has a resolution of 1/40, and AUC is the Mann–Whitney statistic with ties counted as one half.

Uncertainty bands are 10th to 90th percentile ranges over 200 bootstrap replicates, each resampling the nulls once per ensemble (shared across its cells) and each cell's test signals independently before recomputing the thresholds. Censored fractions are recorded, and the bands cover noise and threshold sampling, not the background realization, calibration seed, or model assumptions. CNN uncertainty is the standard deviation across seeds, not a confidence band. The mass proxy converts a cell to free-phase CO_2 mass per area,

$$m_A = h\,\phi\,S_{\mathrm{CO_2}}\,\rho_{\mathrm{CO_2}}(P,T), \tag{8}$$

where P and T are pressure and temperature, with $\rho_{\mathrm{CO_2}} = 683.4$ kg/m^3 at the reference condition, so mass thresholds scale linearly with $\rho_{\mathrm{CO_2}}$ and exclude dissolved CO_2.

Sensitivity design

Each of 13 one-at-a-time variants of the modeling assumptions uses the energy detector, unless the detector is varied, at the default operating point and NRMS 30% and 60%. The axes are the mixing law (Brie, Hill, Voigt), the frame (soft, consolidated), the noise spectrum (tilted low or high), the wavelet phase rotation (removed or doubled), the detector (matched filter, generic template), and the background level (halved, doubled). A factorial crosses the four mixing treatments with the three frames at NRMS 30%. Variants share random numbers with the baseline, and those that change the null chain are recalibrated to the same NRMS. Frame variants keep the baseline deep reflection coefficient and adapt the windows, and bands are suppressed where thresholds are censored.

Two-dimensional transfer check

The transfer check covers 24 cells, 8 thickness–saturation pairs at NRMS 20%, 40%, and 60%, for the energy detector. Each cell has 100 signal realizations, and 1200 nulls per NRMS level are shared across cells. The 1D master scales are reused on the gathers without recalibration, a background of the same construction is drawn independently per trace, and the detection window is shifted by the $1/f_d$ peak delay of the 2D Ricker source. The per-trace test applies the 1D criterion to the zero-offset trace; the section-pooled test computes the energy statistic over about 120 traces around the source, unmigrated and without normal-moveout correction.

Comparison with published Sleipner observations

The comparison uses the Reuss cell at 30 Hz and $S_{CO_2} = 0.8$, with tuning at the thickness of maximum difference amplitude on a coarser sweep. Push-down per net meter of CO_2 is the push-down rate per meter of CO_2-bearing column divided by ϕS_{CO_2}, cumulative push-down is predicted for the two published pairs of column height and push-down, the second for a fully saturated column (Chadwick et al., 2004; Arts et al., 2008), and detectability is compared at NRMS 50%, the closest grid level, and counts as agreeing if the lower end of the energy-detector, matched-filter, and CNN threshold range falls inside the published 0.5–2 m transition (Chadwick et al., 2014). The summary is the largest factor between a prediction and its published value: a published range scores 1 when the prediction falls inside it and otherwise the ratio to its nearer end, and a published bound is scored as a point value even when the prediction satisfies it.

Reproducibility

Monte Carlo draws come from seeded streams keyed by the global seed 42 and the cell coordinates; calibration, bootstrap, 2D modeling, and network training use their own fixed seeds. Dependencies are pinned, and GPU training is not bitwise reproducible, a variation separate from the deliberate seed variation. Scripts write every figure and every number in the text from the results of the full production run; a reduced-size configuration serves only for software testing.

Results

Rock-physics response

At $S_{CO_2} = 0.8$, CO_2 lowers the P-velocity of the Utsira-like sand from 2104 to 1406 m/s under Reuss mixing, a 33.2% drop, and to 1408, 1503, and 1593 m/s under Brie, Hill, and Voigt mixing (Figure 2a). Acoustic impedance falls accordingly (Figure 2d). Under Reuss mixing, 80% of that velocity drop is reached by $S_{CO_2} = 0.1$ and 92% by 0.2, so amplitude constrains saturation poorly.

Tuning and push-down

Measured tuning thicknesses at 15, 30, and 45 Hz, 18.24, 9.10, and 6.06 m, agree with the Ricker-specific predictions of 18.27, 9.13, and 6.09 m within 0.6% (Figure 3d–f), whereas the $\lambda/4$ rule overpredicts them by the factor 1.283. Figure S3 maps the corresponding 4D attributes. Push-down grows linearly at 0.472 ms per meter of CO_2-bearing column (Reuss, $S_{CO_2} = 0.8$), matching the analytic value. Its largest Reuss value is 23.6 ms, at $h = 50$ m and $S_{CO_2} = 0.75$, because the Reuss velocity reaches its minimum at an interior saturation.

The NRMS axis

Median achieved NRMS of the production nulls tracks the calibration targets (Figure 4d). At NRMS 40% and above, the 30- and 45-Hz medians lie +1.8 to +4.9 points from nominal, farthest at 60% and 30 Hz (median 64.9%), which makes their thresholds slightly pessimistic; the 15-Hz medians at 20% and above lie −1.9 to −1.0 points from nominal, so frequency contrasts at nominal 60% if anything understate the 15-Hz

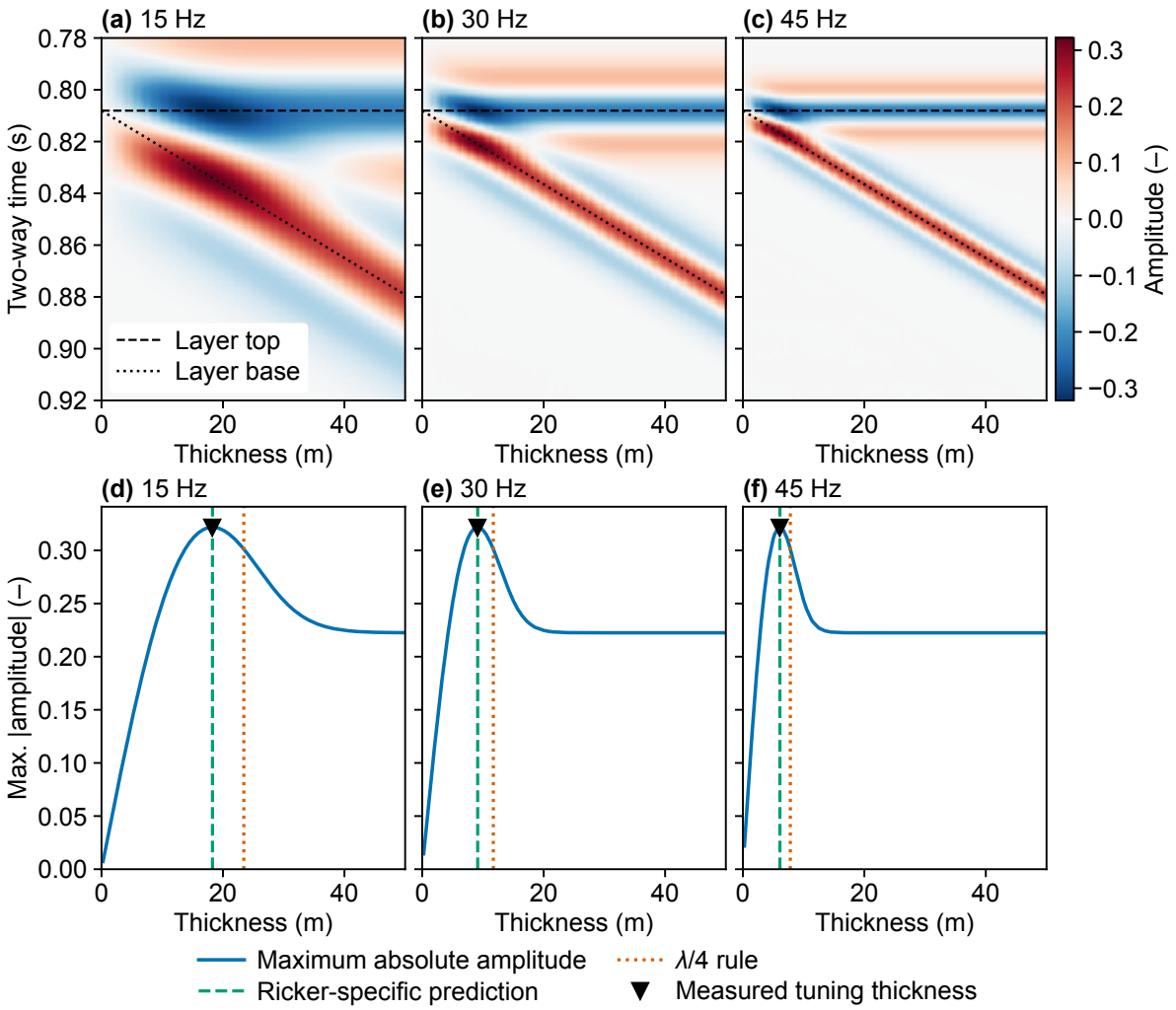


Figure 3. (a–c) Zero-offset wedge traces versus layer thickness at 15, 30, and 45 Hz (Reuss, $S_{CO_2} = 0.8$); (d–f) maximum absolute amplitude versus thickness with the measured tuning thickness, the Ricker-specific prediction, and the $\lambda/4$ rule.

penalty. At nominal 60% and 30 Hz, single realizations span 39–120% between the 10th and 90th percentiles (Figure S4), so each threshold integrates over a broad spread of per-realization NRMS.

Detection statistics and probability maps

At NRMS 30%, null and plume distributions separate for the 6-m cell and overlap for the 1-m cell, more for the energy detector than for the matched filter (Figure 5). In the marginal 2-m cell the energy detector's plume distribution straddles the threshold and its detection probability just clears 0.9, so small shifts can flip the outcome; Figure S5 gives the receiver operating characteristic curves.

The detection frontier, the 0.9 contour, moves to thicker layers as NRMS rises and stays at nearly constant thickness above the lowest saturations (Figure 6; Figures S6 and S7 for 15 and 45 Hz). The matched-filter frontier fragments at NRMS $\geq$ 50% because its detection probability is not monotone in thickness: all 6 of

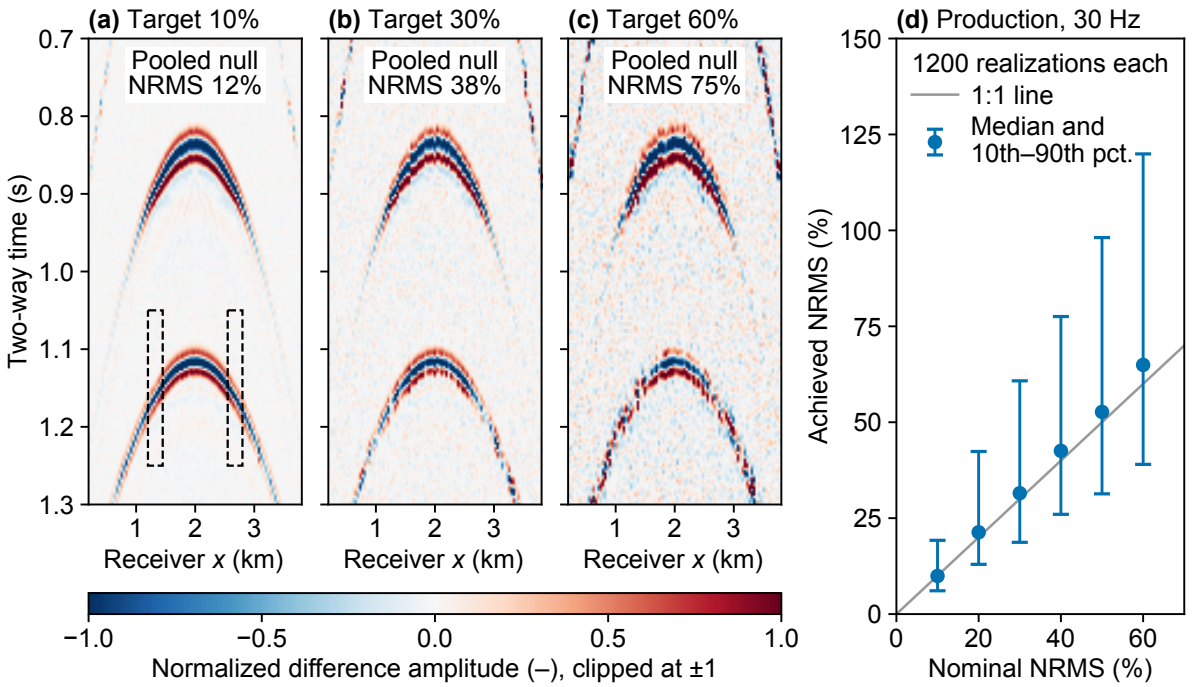


Figure 4. (a–c) 2D difference gathers at target NRMS 10%, 30%, and 60% with the production master scales, annotated with the section-pooled NRMS of baseline-only survey pairs in the dashed windows of (a); (d) achieved versus nominal NRMS of the 30-Hz production null ensembles (median, 10th–90th percentiles of 1200 realizations).

its per-saturation curves at NRMS 60% (3 of 6 at 50%) fall back below the target after first crossing it, so the first-crossing rule favors the matched filter there.

Detectability thresholds

Minimum detectable thickness rises with NRMS for every detector (Table 1; Figure 7a), for the energy detector from 1.0 m, censored at the grid floor, at NRMS 10% to 4.5 m at NRMS 60%. At NRMS 60% the matched filter reaches 6.0 m, the CNN 3.1 m, and the generic-template filter 15.0 m; censoring makes the rise a lower bound. The smallest detectable energy-detector mass per area rises from 25 to 253 kg/m^2, the lower value a censored grid corner (Figure 7b). The mass minimum lies at the lowest tested saturation, $S_{CO_2} = 0.1$, in 51 of the 54 combinations of non-CNN detector, frequency, and NRMS, so it is censored there and holds under Reuss mixing only, whereas the thickness thresholds belong to $S_{CO_2} = 0.8$. At NRMS 60% the matched filter has the lowest mass, 101 kg/m^2, against 126 for the CNN and 253 for the energy detector, because it keeps sensitivity to thin, low-saturation layers.

Higher dominant frequency lowers the threshold, consistent with tuning: at NRMS 60% the energy threshold is 10.0, 4.5, and 2.7 m at 15, 30, and 45 Hz (Figure 7c, d). Moving to $P_{FA} = 0.01$ raises the energy threshold most at NRMS 60%, from 4.5 to 6.3 m. Typical bootstrap half-widths are 0.1–0.6 m; among bands without censored replicates the widest are the generic template's at NRMS 50% (5.6 m below) and the matched filter's at NRMS 60% (−3.0/+1.0 m). The CNN seed standard deviation is at most 0.14 m at 30 Hz and 0.17 m overall (Figure S8), and 1.30 m at $P_{FA} = 0.01$ (15 Hz, NRMS 60%). Reevaluating the energy and

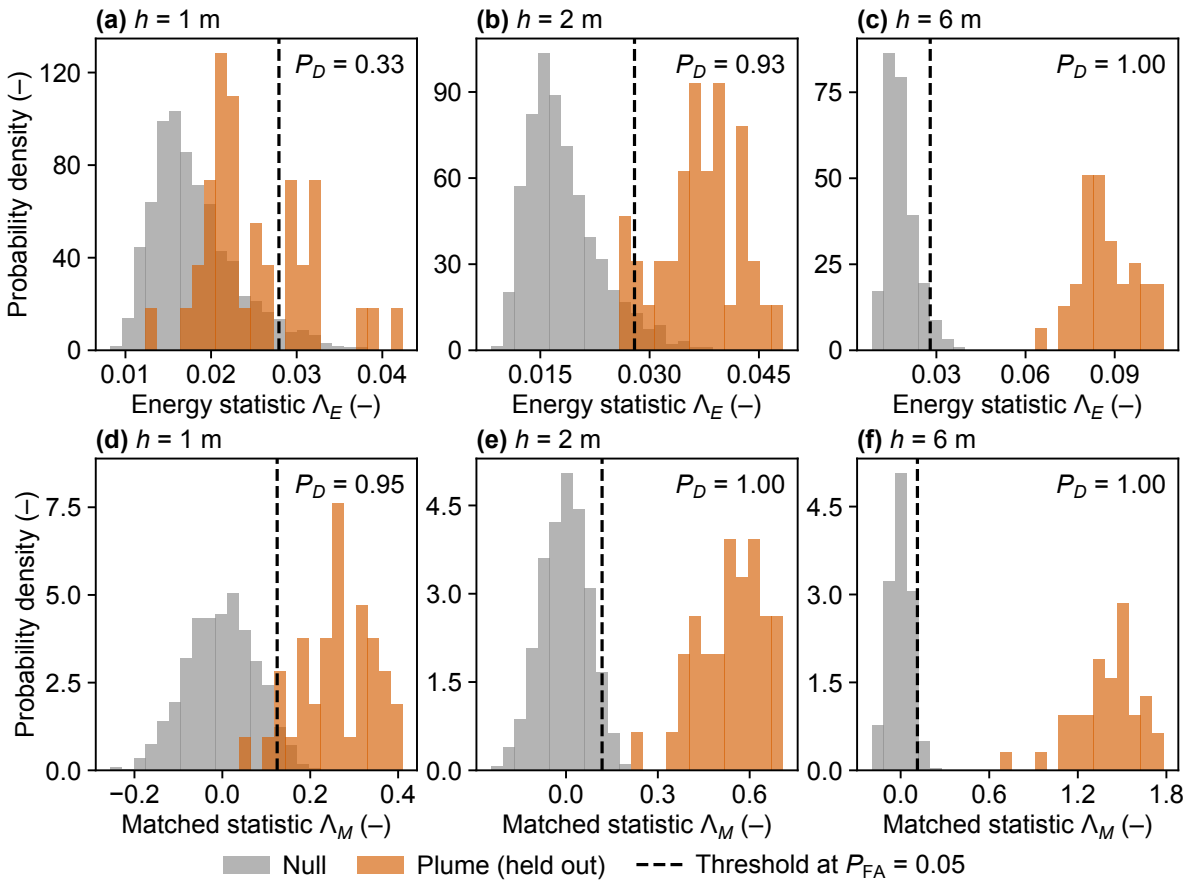


Figure 5. Null (gray, 1200) and plume (orange, 40 held-out) histograms of the (a–c) energy and (d–f) matched statistics for cells with h = 1, 2, and 6 m (NRMS 30%, 30 Hz, S_{CO_2} = 0.8); dashed lines: threshold at P_{FA} = 0.05.

Table 1. Minimum detectable CO_2 layer thickness (m) at S_{CO_2} = 0.8, $P_D \geq 0.9$, P_{FA} = 0.05, and 30 Hz. †Censored at the 1-m grid floor; detection may extend to thinner layers. "Mismatched" denotes the generic-template filter.

NRMS (%)	Energy	Matched	CNN	Mismatched
10	1.0†	1.0†	1.0†	2.8
20	1.8	1.0†	1.0†	4.0
30	2.0	1.0†	1.2	5.5
40	2.7	1.6	1.9	8.0
50	3.0	1.8	2.0	14.3
60	4.5	6.0	3.1	15.0

matched detectors on all 150 realizations at the default operating point shifts thresholds by at most 0.52 m (energy detector, NRMS 50%), always inside the bootstrap band.

Template correlation under nonrepeatability

At 30 and 45 Hz the clean-template matched filter loses its AUC advantage as NRMS rises; at 15 Hz it keeps it across the axis. At NRMS $\leq$ 30%, the expected ordering of matched filter, CNN, and energy detector has 4 exceptions among 864 cells at a 0.02 AUC margin, most near perfect discrimination. The

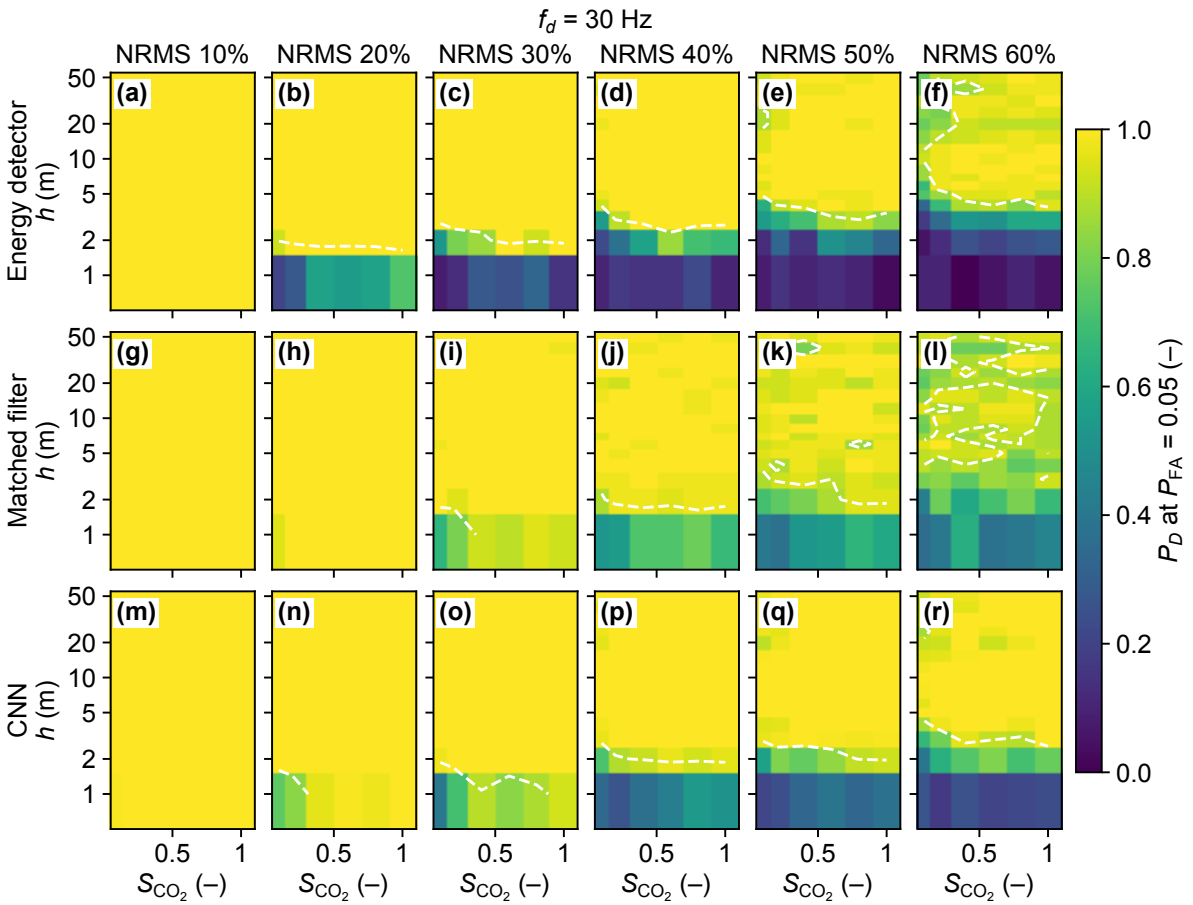


Figure 6. Detection probability at $P_{FA} = 0.05$ over thickness and saturation at 30 Hz for the (a–f) energy detector, (g–l) matched filter, and (m–r) CNN at six NRMS levels; dashed contours mark $P_D = 0.9$; CNN values are means over 3 seeds.

energy detector and the CNN beat the matched filter by more than 0.02 in AUC in 226 and 281 of 1728 cells, and of the 372 energy wins at any margin, 366 lie at NRMS ≥ 40%. With 40 test realizations the matched-filter AUC in these cells has a median standard error of 0.02 (Hanley and McNeil, 1982), comparable to the margin, so the counts are descriptive; their structure is the evidence: 2, 90, and 134 energy exceedances lie at 15, 30, and 45 Hz; in 213 of them the energy detector's operating-point detection probability also matches or exceeds the matched filter's; and the CNN wins in 166 of the 288 NRMS-60% cells. In the cell with the largest gap (45 Hz, NRMS 60%, $h = 2$ m, $S_{CO_2} = 1.0$), the matched filter reaches an AUC of 0.78, against 0.98 for the energy detector and 1.00 for the CNN. Per-trace static shifts, whose standard deviation at NRMS 60% grows from 5% of the dominant period at 15 Hz to 11% at 45 Hz, would decorrelate a zero-lag template but not an rms statistic, a mechanism not isolated here.

The detector ordering at 30 Hz and NRMS 60%, with the CNN lowest, is not resolved: the matched filter's lower band, 3.0 m below its threshold, reaches below both other thresholds, and its detection probability stays between 0.75 and 0.83 from 2 to 5 m before it crosses, so a slightly lower target would reorder the detectors. The CNN's in-distribution thickness advantage at NRMS 60% holds at 45 Hz (1.4 against the matched filter's 2.0 m), but at 15 Hz the matched filter has the lower threshold (6.4 against 6.9 m). The generic-template filter

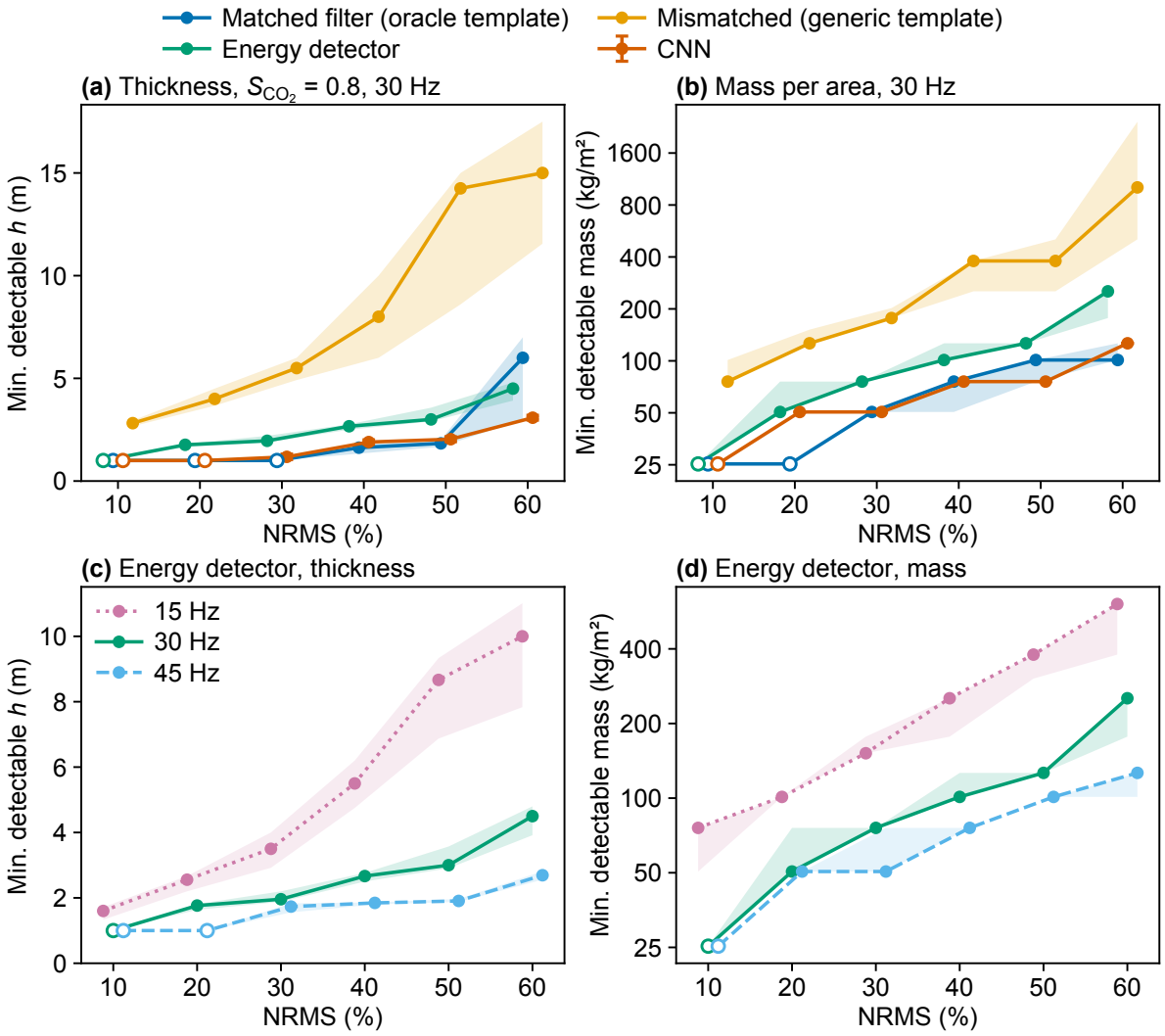


Figure 7. Minimum detectable (a) thickness at S_{CO_2} = 0.8 and (b) mass per area versus NRMS for four detectors at 30 Hz; (c, d) the same for the energy detector at three frequencies. Masses are grid minima, nearly always at the lowest saturation. Bands are bootstrap 10th–90th percentiles; CNN error bars are ±1 standard deviation across 3 seeds; open markers are censored; series are offset slightly in NRMS for legibility; "mismatched" is the generic template.

is weakest in nearly every cell, with a 30-Hz threshold 2–8 times the matched filter's and 2–5 times the energy detector's. Its AUC exceeds the matched filter's in only 12 of 576 cells at 30 Hz (Figure S9).

Transfer from 1D traces to 2D gathers

Detection statistics from the 1D grid agree with the 2D gathers (Figure 8) once thickness quantization is accounted for. The 24 cells have a mean AUC difference (2D minus 1D) of +0.022 and a Spearman rank correlation of 0.889, with ties where cells saturate in both. The positive mean comes from the quantized 1-m cells: the worst (h = 1 m, NRMS 60%) has an AUC of 0.59 in 1D and 0.83 in 2D, and without the 1-m cells the mean difference is +0.002. Detect-or-not calls differ in 3 cells: the 1-m cell at NRMS 20% is detected only in 2D, and the 5-m and 25-m cells at NRMS 60% only in 1D, so 1D thresholds may be slightly optimistic at high NRMS. The section-pooled test discriminates perfectly in every cell, from about 120 traces, whose square root gives an idealized, unmeasured signal-to-noise gain of about 11 for laterally independent noise, an upper bound.

Sensitivity to modeling assumptions

A consolidated host suppresses detection over the whole thickness grid at both tested NRMS levels, censoring the threshold beyond the 50-m grid maximum (Figure 9). At h = 2 m its AUC is 0.41 at NRMS 30% and 0.50 at 60%, within about two standard errors (0.05 near one half; Hanley and McNeil, 1982) of chance, consistent with the consolidated sandstone's 5% velocity drop at S_{CO_2} = 0.8 (Figure 2e–h); it marks a different site class, not a parameter uncertainty. Against baselines of 1.96 and 4.5 m at NRMS 30% and 60% (Table 1 values at higher display precision), the soft frame shifts the threshold by −0.21 and −1.75 m.

Within the Utsira-like site the ranking depends on NRMS. At NRMS 30% (Figure 9a), the generic template raises the threshold by +3.54 m and a doubled background by +2.04 m, while the matched filter and a halved background shift it by −0.96 and −0.96 m, bounds because both reach the grid floor. Voigt, Hill, and Brie mixing shift it by +0.92, +0.60, and +0.00 m; the phase-rotation and noise-spectrum variants move it by at most 0.11 and 0.10 m, less than the 0.45-m width of the baseline bootstrap band of the sensitivity runs (Figure S10a), so these shifts are not resolved. At NRMS 60% (Figure 9b) the generic template adds +10.5 m, Voigt mixing +4.8 m, and a doubled background censors the threshold. The matched-filter swap now raises the threshold, by +1.5 m, the reversal seen in Table 1; a halved background shifts it by −1.9 m, and the phase-rotation and noise-spectrum variants by at most 0.65 m. In the NRMS-30% factorial the Voigt penalty is 0.92 m in the Utsira-like frame but 0.25 m in the soft frame (Figure S10).

Consistency with published Sleipner observations

Predictions agree with published Sleipner values within a factor of 1.41 on 11 observables (Figure 10b), a consistency check, not validation. That factor comes from a cumulative push-down of 42.3 ms that satisfies a published lower bound of more than 30 ms (Arts et al., 2008); against published point values the worst pair is another push-down, 28.3 ms predicted against 22 ms (Chadwick et al., 2004). Six observables echo the rock parameterization: the CO_2-sand velocity, 1406 m/s, lies below the published 1464–1474 m/s (Williams and Chadwick, 2012); the velocity reduction, 33.2%, slightly above the published upper bound of 30% (Arts et al., 2008); the Reuss acoustic impedances, 4.32 and 2.75 $\times 10^6$ kg/(m^2 s), close to the published values (above

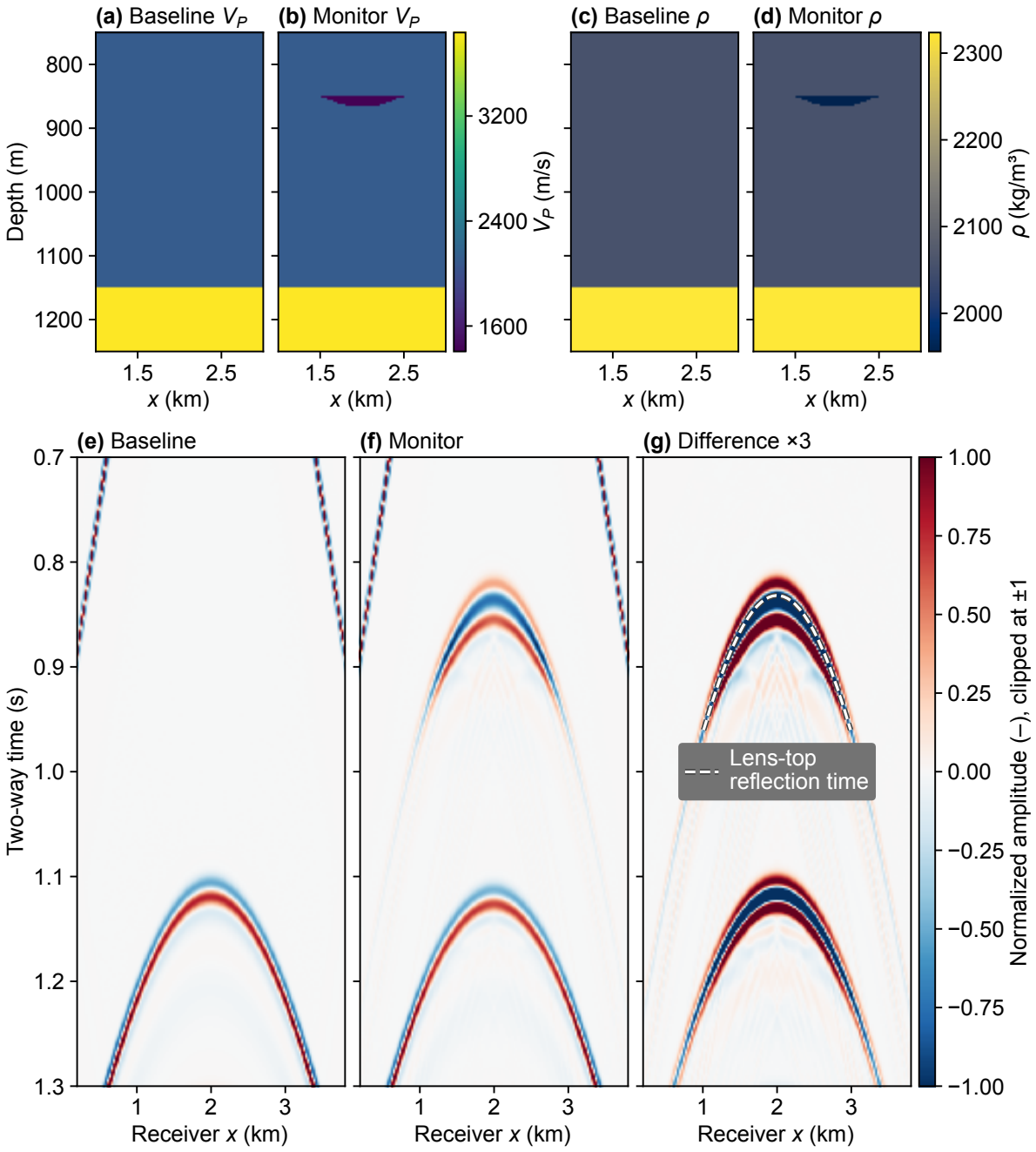


Figure 8. (a, b) Baseline and monitor P-velocity and (c, d) density with a lens-shaped plume; common-shot gathers of the (e) baseline, (f) monitor, and (g) amplified difference, which shows the plume response at the reservoir and push-down at the deep reflector; dashed: predicted lens-top reflection time; the clipped steep events at the upper corners of (e) and (f) are the direct arrival.

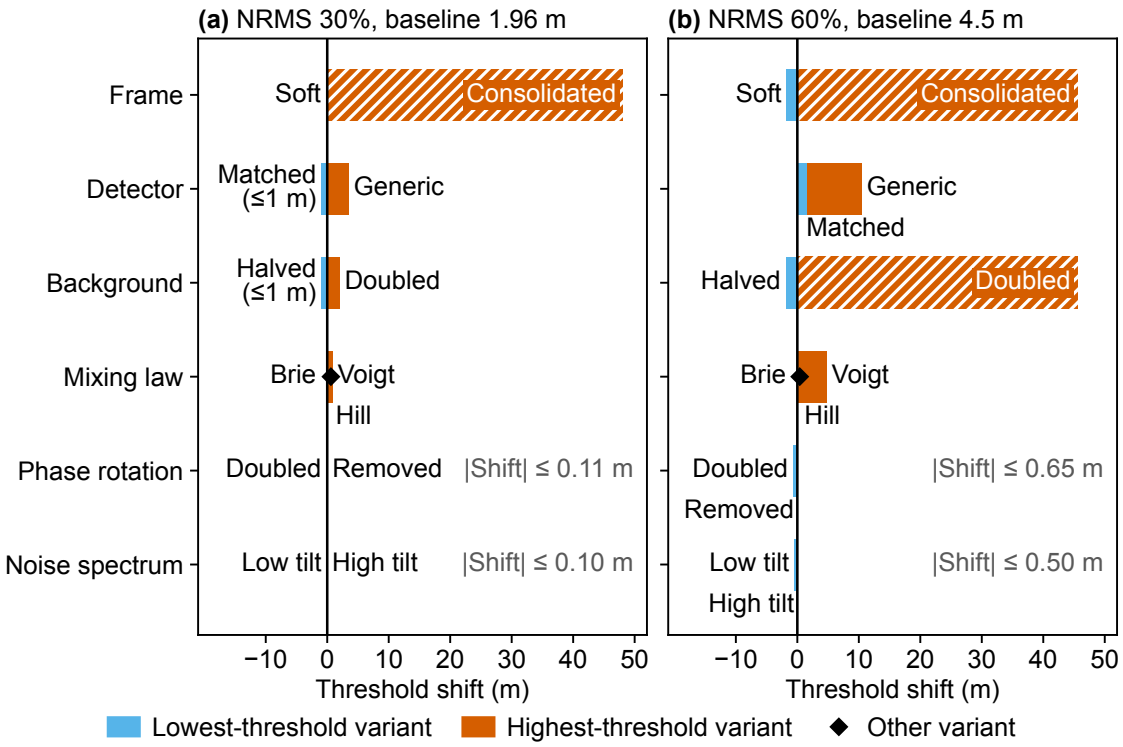


Figure 9. Threshold shift when each assumption is varied alone (energy detector, 30 Hz, $S_{CO_2} = 0.8$, $P_{FA} = 0.05$), at (a) NRMS 30% and (b) NRMS 60%; the diamond marks Hill mixing. Hatched bars are censored at the 50-m grid maximum.

for brine sand, below for CO_2 sand) (Williams and Chadwick, 2012); the impedance ratio, 0.636, slightly above a published upper bound of 0.625 (Chadwick et al., 2010); and the top-layer reflection coefficient, $R_{top} = -0.222$, whose magnitude lies somewhat above the published-derived 0.191 (Williams and Chadwick, 2012). Most of these offsets indicate a stronger CO_2 effect than observed, consistent with Reuss mixing being the favorable case.

The other five are less directly tied to the inputs, although tuning and push-down still depend on the predicted CO_2-sand velocity. The tuning thickness, 9.0 m, lies above the published 7.5–8.0 m (Chadwick et al., 2010; Arts et al., 2008), and the push-down rate, 1.59 ms per net meter of CO_2, within the published range at high saturation (Chadwick et al., 2004). The published 22-ms push-down (Chadwick et al., 2004) lies between the Reuss and Voigt predictions, closer to Voigt (Figure 10a), so the comparison does not exclude the mixing law that raises thresholds. Published Sleipner survey pairs, with average NRMS of 45% and 53% (Jun and Cho, 2022), lie toward the high end of the studied axis, and cross-equalization improves one pair from 65% to 56% (Singh et al., 2025). At NRMS 50% the energy-detector, matched-filter, and CNN thresholds span 1.8–3.0 m, with the CNN at 2.0 m. For minimum detectable thickness, the fifth of these observables, Chadwick et al. (2014) report that layers thicker than 2 m are readily detectable and that layers thinner than 0.5 m are difficult to detect. Published mass thresholds of 500 and 2100 t are total accumulations, not comparable to per-area values (Chadwick et al., 2006, 2014).

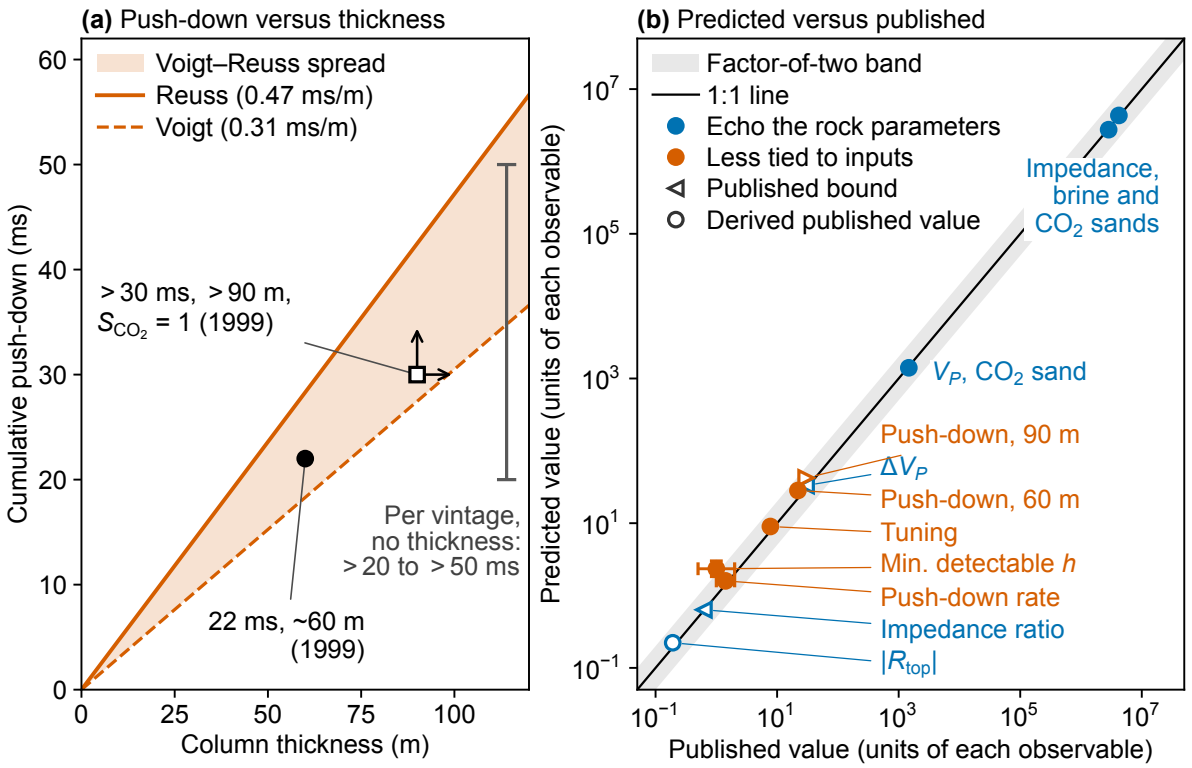


Figure 10. (a) Predicted cumulative push-down versus column thickness (Reuss and Voigt) with published Sleipner observations; (b) predicted versus published values for the 11 observables, with a 1:1 line and a factor-of-two band (sources cited in the text); the gray bar in (a) is the per-vintage push-down range (Chadwick et al., 2004; Arts et al., 2008; Bergmann and Chadwick, 2015), which has no paired thickness. In (b), triangles point toward the open side of a one-sided published bound, and error bars span published (horizontal) and predicted (vertical) ranges. Panel b spans decades and mixed units; all predictions lie within a factor of 1.41 of published values.

Discussion

Published Sleipner NRMS lies between the 40% and 60% grid levels (Jun and Cho, 2022); at NRMS 50%, the 30-Hz Reuss thresholds of the energy detector, matched filter, and CNN span 1.8–3.0 m (Figure 7a). Cross-equalization moved one published pair into the studied range (Singh et al., 2025), so the processing state belongs with NRMS in any threshold claim. The estimate serves design, not field calibration: the Sleipner comparison tests mainly response magnitudes, and its one threshold observable is scored by range overlap and agrees in direction only. The published push-down lies closer to the Voigt prediction, which adds +4.8 m to the NRMS-60% threshold, and the published averages do not report the perturbation composition the axis assumes. The chart is the controlled baseline against which a field program would calibrate its own detection claims.

At 30 Hz, repeatability moves the threshold more than the choice of detector: improving NRMS from 60% to 30% lowers the energy threshold from 4.5 to 2.0 m, more than the best detector change at NRMS 60% (the CNN, at 3.1 m), although that detector ordering is itself not resolved. At 45 Hz the repeatability gain, from 2.7 to 1.7 m, no longer exceeds the best detector change (the CNN, at 1.4 m). Halving the dominant

frequency from 30 to 15 Hz moves the NRMS-60% energy threshold from 4.5 to 10.0 m, more than either (Figure 7c).

Single-trace thresholds translate into an under-mapped plume margin. For a lens with the thickness profile of equation 2 and center thickness $h \geq h_{\min}$, traces with $H(x) \geq h_{\min}$ meet the detection target out to the detected half-width

$$x_d = L\sqrt{1 - h_{\min}/h} \tag{9}$$

from the lens center. For $h \gg h_{\min}$, the undetected rim on each side is close to $L\,h_{\min}/(2h)$ wide, so it widens as NRMS rises or frequency falls. This assumes uniform saturation and per-trace decisions; lateral coherence would recover part of the loss.

Template detection is only as good as the time alignment that precedes it. The matched-filter reversal at NRMS 60% (Figure 9b) reuses the realizations of Table 1, so it is not independent evidence. Cross-equalizing and time-aligning a survey pair before correlating it with a type response moves the data toward the premise under which the matched filter is optimal (Kay, 1998); detectors that search over arrival time, the generalized likelihood ratio test for an unknown delay (Kay, 1998), and templates whitened for the band-limited noise are untested alternatives.

Two survey pairs with the same NRMS can differ in detectability. Doubling the in-window background raises the NRMS-30% energy threshold (Figure 9a) and suppresses detection at NRMS 60%, a consolidated host suppresses energy detection at both levels, and the share of statics in the mix, whose perturbations operate at several times their unit-mix values at high NRMS, was not varied. A threshold claim therefore needs the target geology and noise composition as well as NRMS.

Relative to lateral coherence alone, single-trace thresholds are conservative: the section-pooled test, an idealized upper bound, discriminated perfectly. Against the optimistic idealizations listed under Limitations, the net direction for field interpretation is not known. The field transition implied by Chadwick et al. (2014) lies at or below the single-trace range at NRMS 50%, consistent with a coherence gain, but the agreement is in direction only. Because published NRMS values are survey-pair averages and this study quotes per-trace-pair medians, the field probably sits somewhat lower on the studied axis.

Unlike the Aquistore studies, which ask what clears an empirical noise floor (Roach et al., 2015, 2017), and the leakage scenarios of Wang et al. (2018), these thresholds are null-calibrated at a fixed false-alarm probability and swept across NRMS for four detectors; they address detection, whereas full-wavefield imaging of the Sleipner plume (Martinez et al., 2026) addresses characterization.

Limitations

Every threshold is conditional on these idealizations, with the expected direction of bias where known. The physics is acoustic, without elastic offset effects (including at the moderate offsets of the pooled test), converted waves, or attenuation, and the geometry is 1D and 2D, without a 3D wavefield or migration. The noise is synthetic, stationary, and parametric, without coherent noise, multiples, or geometry nonrepeatability, which makes the thresholds optimistic. No cross-equalization precedes detection, and the NRMS axis stands for residual repeatability with a composition fixed by the unit mix. The reported thresholds use Reuss mixing, which with Brie mixing gives the lowest thresholds of the four treatments; the mixing law is quan-

tified but not resolved, and saturation is poorly identifiable from amplitudes. The in-window background level is an unconstrained parameter with a first-order effect that partly stands in for the excluded intrareservoir mudstones, and injection-driven changes in pore pressure and their effect on the frame are not modeled. The mass proxy counts free-phase CO_2 only. The model holds one CO_2 layer in a homogeneous host, with primaries only and no stacked-layer interference, so it describes an isolated or topmost layer at reservoir conditions, not a shallow gaseous accumulation. Excluding the deep-reflector push-down from detection is conservative for thick columns.

For the detection criterion, the known window of the single-trace test makes it optimistic, survey-level false-alarm control would raise thresholds, and lateral pooling would lower them; field interpreters also gain from processing and lose to coherent noise and limited amplitude fidelity. Outcomes were not regressed on per-realization NRMS. The CNN is a small, fixed architecture evaluated across 3 seeds and trained and tested on one noise model and background, so its result holds in distribution only and is optimistic with respect to field transfer; a network trained on preinjection field surveys instead learns the site's own nonrepeatability (Park et al., 2024). Every generic-template result rests on one reference cell, and at high NRMS the matched-filter threshold depends on the target detection probability. One background realization per frequency is shared by all detectors and by the CNN's training and test data, so the bands omit between-geology variability and frequency contrasts are partly confounded with the background draw. The 2D check covers only the energy detector, with quantized thickness, at equal master scale rather than equal achieved NRMS. Some attributions rest on secondary sources or independent reproductions rather than primary full text: the quartz moduli (Mavko et al., 2009), the salinity corroboration (Portier and Rochelle, 2005), the cross-equalization NRMS values (Singh et al., 2025), the attribution of the peak-to-trough tuning criterion (Kallweit and Wood, 1982), and the NRMS and brine formulas (Kragh and Christie, 2002; Batzle and Wang, 1992); resolving them would not change a threshold reported for the Utsira-like sand.

Suggestions for further study

Elastic, 3D, and migrated modeling with patchy-saturation calibration and pressure effects would approach field physics, and empirical coherent noise, a processing step, and replicated backgrounds would test how far NRMS alone predicts detectability. Joint amplitude and traveltime criteria that include push-down, survey-level false-alarm control, and synthetic-to-field CNN transfer with null calibration remain to be evaluated.

Conclusion

A seismic CO_2 detection limit is a function of repeatability, false-alarm probability, detector, frequency, and fluid-mixing law, not a single number. Under uniform mixing, worsening repeatability alone carries the 30-Hz single-trace energy-detector threshold from the grid floor to 4.5 m at NRMS 60%. At that operating point, halving the dominant frequency moved the threshold more than halving NRMS did, and stricter false-alarm control raised it.

Signature knowledge pays only while repeatability preserves the signal's alignment. At higher frequency and poor repeatability, a zero-lag clean-template correlator lost its advantage over the energy detector and

the CNN, consistent with misalignment, but kept it at the lowest frequency; how far this carries to field data depends on a nonrepeatability composition that NRMS alone does not report. A CNN trained on the expected noise often did best at high NRMS, an in-distribution result, and the generic template was weakest. In-window reflectivity and host-rock stiffness also set detectability, and a consolidated host can hide the signal across the modeled thickness range.

Predictions agree with published Sleipner values within a factor of 1.41 on 11 observables, a consistency check rather than validation. The thresholds describe an isolated acoustic layer at Utsira-like conditions under a single-trace, known-window criterion; lateral coherence would lower them, while the known window and stationary noise make them optimistic. A credible monitoring claim states the repeatability, the false-alarm probability, and the detector together.

Funding

This research received no specific funding.

Data and materials availability

The study is fully synthetic: no proprietary data were used, and field information enters only through published Sleipner values cited in the text. The code that generates every result and figure is available from the author on request.

References

Arts, R. J., A. Chadwick, O. Eiken, S. Thibeau, and S. Nooner, 2008, Ten years' experience of monitoring CO_2 injection in the Utsira Sand at Sleipner, offshore Norway: First Break, **26**, 65–72, doi: 10.3997/1365-2397.26.1115.27807.

Arts, R., O. Eiken, A. Chadwick, P. Zweigel, L. van der Meer, and B. Zinszner, 2004, Monitoring of CO_2 injected at Sleipner using time-lapse seismic data: Energy, **29**, 1383–1392, doi: 10.1016/j.energy.2004.03.072.

Audigane, P., I. Gaus, I. Czernichowski-Lauriol, K. Pruess, and T. Xu, 2007, Two-dimensional reactive transport modeling of CO_2 injection in a saline aquifer at the Sleipner site, North Sea: American Journal of Science, **307**, 974–1008, doi: 10.2475/07.2007.02.

Batzle, M., and Z. Wang, 1992, Seismic properties of pore fluids: GEOPHYSICS, **57**, 1396–1408, doi: 10.1190/1.1443207.

Bell, I. H., J. Wronski, S. Quoilin, and V. Lemort, 2014, Pure and pseudo-pure fluid thermophysical property evaluation and the open-source thermophysical property library CoolProp: Industrial & Engineering Chemistry Research, **53**, 2498–2508, doi: 10.1021/ie4033999.

Bergmann, P., and A. Chadwick, 2015, Volumetric bounds on subsurface fluid substitution using 4D seismic time shifts with an application at Sleipner, North Sea: GEOPHYSICS, **80**, no. 5, B153–B165, doi: 10.1190/geo2014-0591.1.

Brie, A., F. Pampuri, A. F. Marsala, and O. Meazza, 1995, Shear sonic interpretation in gas-bearing sands: SPE Annual Technical Conference and Exhibition, SPE-30595-MS, doi: 10.2118/30595-MS.

Carcione, J. M., S. Picotti, D. Gei, and G. Rossi, 2006, Physics and seismic modeling for monitoring CO_2 storage: Pure and Applied Geophysics, **163**, 175–207, doi: 10.1007/s00024-005-0002-1.

Chadwick, A., R. Arts, O. Eiken, P. Williamson, and G. Williams, 2006, Geophysical monitoring of the CO_2 plume at Sleipner, North Sea, in S. Lombardi, L. K. Altunina, and S. E. Beaubien, eds., Advances in the geological storage of carbon dioxide: Springer, NATO Science Series IV: Earth and Environmental Sciences, 303–314, doi: 10.1007/1-4020-4471-2_25.

Chadwick, A., G. Williams, N. Delepine, V. Clochard, K. Labat, S. Sturton, M.-L. Buddensiek, M. Dillen, M. Nickel, A. L. Lima, R. Arts, F. Neele, and G. Rossi, 2010, Quantitative analysis of time-lapse seismic monitoring data at the Sleipner CO_2 storage operation: The Leading Edge, **29**, 170–177, doi: 10.1190/1.3304820.

Chadwick, R. A., R. Arts, O. Eiken, G. A. Kirby, E. Lindeberg, and P. Zweigel, 2004, 4D seismic imaging of an injected CO_2 plume at the Sleipner Field, central North Sea, in 3D seismic technology: Application to the exploration of sedimentary basins: Geological Society, London, Memoirs 29, 311–320, doi: 10.1144/GSL.MEM.2004.029.01.29.

Chadwick, R. A., B. P. Marchant, and G. A. Williams, 2014, CO_2 storage monitoring: Leakage detection and measurement in subsurface volumes from 3D seismic data at Sleipner: Energy Procedia, **63**, 4224–4239, doi: 10.1016/j.egypro.2014.11.458.

Dupuy, B., A. Romdhane, P. Eliasson, E. Querendez, H. Yan, V. A. Torres, and A. Ghaderi, 2017, Quantitative seismic characterization of CO_2 at the Sleipner storage site, North Sea: Interpretation, **5**, no. 4, SS23–SS42, doi: 10.1190/INT-2017-0013.1.

Furre, A.-K., O. Eiken, H. Alnes, J. N. Vevatne, and A. F. Kiær, 2017, 20 years of monitoring CO_2-injection at Sleipner: Energy Procedia, **114**, 3916–3926, doi: 10.1016/j.egypro.2017.03.1523.

Gassmann, F., 1951, Über die Elastizität poröser Medien: Vierteljahrsschrift der Naturforschenden Gesellschaft in Zürich, **96**, 1–23.

Ghaderi, A., and M. Landrø, 2009, Estimation of thickness and velocity changes of injected carbon dioxide layers from prestack time-lapse seismic data: GEOPHYSICS, **74**, no. 2, O17–O28, doi: 10.1190/1.3054659.

Han, D.-H., 1986, Effects of porosity and clay content on acoustic properties of sandstones and unconsolidated sediments: Ph.D. thesis, Stanford University.

Hanley, J. A., and B. J. McNeil, 1982, The meaning and use of the area under a receiver operating characteristic (ROC) curve: Radiology, **143**, 29–36, doi: 10.1148/radiology.143.1.7063747.

Harvey, S., J. Hopkins, H. Kuehl, S. O'Brien, and A. Mateeva, 2022, Quest CCS facility: Time-lapse seismic campaigns: International Journal of Greenhouse Gas Control, **117**, 103665, doi: 10.1016/j.ijggc.2022.103665.

Ivanova, A., A. Kashubin, N. Juhojuntti, J. Kummerow, J. Henninges, C. Juhlin, S. Lüth, and M. Ivandic, 2012, Monitoring and volumetric estimation of injected CO_2 using 4D seismic, petrophysical data, core measurements and well logging: A case study at Ketzin, Germany: Geophysical Prospecting, **60**, 957–973, doi: 10.1111/j.1365-2478.2012.01045.x.

Jenkins, C., A. Chadwick, and S. D. Hovorka, 2015, The state of the art in monitoring and verification: Ten years on: International Journal of Greenhouse Gas Control, **40**, 312–349, doi: 10.1016/j.ijggc.2015.05.009.

Jun, H., and Y. Cho, 2022, Repeatability enhancement of time-lapse seismic data via a convolutional autoencoder: Geophysical Journal International, **228**, 1150–1170, doi: 10.1093/gji/ggab397.

Kallweit, R. S., and L. C. Wood, 1982, The limits of resolution of zero-phase wavelets: GEOPHYSICS, **47**, 1035–1046, doi: 10.1190/1.1441367.

Kay, S. M., 1998, Fundamentals of statistical signal processing, volume II: Detection theory: Prentice-Hall PTR.

Kolkman-Quinn, B., D. C. Lawton, and M. Macquet, 2023, CO_2 leak detection threshold using vertical seismic profiles: International Journal of Greenhouse Gas Control, **123**, 103839, doi: 10.1016/j.ijggc.2023.103839.

Kragh, E., and P. Christie, 2002, Seismic repeatability, normalized rms, and predictability: The Leading Edge, **21**, 640–647, doi: 10.1190/1.1497316.

Landrø, M., 2001, Discrimination between pressure and fluid saturation changes from time-lapse seismic data: GEOPHYSICS, **66**, 836–844, doi: 10.1190/1.1444973.

Louboutin, M., M. Lange, F. Luporini, N. Kukreja, P. A. Witte, F. J. Herrmann, P. Velesko, and G. J. Gorman, 2019, Devito (v3.1.0): An embedded domain-specific language for finite differences and geophysical exploration: Geoscientific Model Development, **12**, 1165–1187, doi: 10.5194/gmd-12-1165-2019.

Lumley, D., 2010, 4D seismic monitoring of CO_2 sequestration: The Leading Edge, **29**, 150–155, doi: 10.1190/1.3304817.

Lumley, D. E., R. A. Behrens, and Z. Wang, 1997, Assessing the technical risk of a 4-D seismic project: The Leading Edge, **16**, 1287–1292, doi: 10.1190/1.1437784.

Luporini, F., M. Louboutin, M. Lange, N. Kukreja, P. Witte, J. Hückelheim, C. Yount, P. H. J. Kelly, F. J. Herrmann, and G. J. Gorman, 2020, Architecture and performance of Devito, a system for automated stencil computation: ACM Transactions on Mathematical Software, **46**, 6, doi: 10.1145/3374916.

Martinez, R., V. Vinje, H. Moore, S. Hollingworth, P. Ringrose, and A. Stovas, 2026, Unraveling multilayer CO_2 plumes using the entire wavefield: Case study from the Sleipner storage site: Interpretation, **14**, no. 2, T163–T183, doi: 10.1190/int-2025-0016.

Mavko, G., T. Mukerji, and J. Dvorkin, 2009, The rock physics handbook, 2nd ed.: Cambridge University Press.

Park, M. J., J. Frigerio, B. Clapp, and B. Biondi, 2024, DeepNRMS: Unsupervised deep learning for noise-robust CO_2 monitoring in time-lapse seismic images: GEOPHYSICS, **89**, no. 4, IM1–IM11, doi: 10.1190/geo2023-0608.1.

Portier, S., and C. Rochelle, 2005, Modelling CO_2 solubility in pure water and NaCl-type waters from 0 to 300 °C and from 1 to 300 bar: Application to the Utsira Formation at Sleipner: Chemical Geology, **217**, 187–199, doi: 10.1016/j.chemgeo.2004.12.007.

Roach, L. A. N., D. A. Angus, and D. J. White, 2017, Assessment of the limitations on the seismic detectability of injected CO_2 within a deep geological reservoir: Energy Procedia, **114**, 4008–4019, doi: 10.1016/j.egypro.2017.03.1541.

Roach, L. A. N., and D. J. White, 2018, Evolution of a deep CO_2 plume from time-lapse seismic imaging at the Aquistore storage site, Saskatchewan, Canada: International Journal of Greenhouse Gas Control, **74**, 79–86, doi: 10.1016/j.ijggc.2018.04.025.

Roach, L. A. N., D. J. White, and B. Roberts, 2015, Assessment of 4D seismic repeatability and CO_2 detection limits using a sparse permanent land array at the Aquistore CO_2 storage site: GEOPHYSICS, **80**, no. 2, WA1–WA13, doi: 10.1190/geo2014-0201.1.

Sheriff, R. E., 2002, Encyclopedic dictionary of applied geophysics, 4th ed.: Society of Exploration Geophysicists, Geophysical References Series 13, doi: 10.1190/1.9781560802969.

Singh, A. P., S. P. Maurya, R. Kant, K. H. Singh, R. Singh, M. K. Srivastava, G. Hema, and N. Verma, 2025, Implementing 4D seismic inversion based on linear programming techniques for CO_2 monitoring at the Sleipner field CCS site in the North Sea: Acta Geophysica, **73**, 271–293, doi: 10.1007/s11600-024-01376-6.

Span, R., and W. Wagner, 1996, A new equation of state for carbon dioxide covering the fluid region from the triple-point temperature to 1100 K at pressures up to 800 MPa: Journal of Physical and Chemical Reference Data, **25**, 1509–1596, doi: 10.1063/1.555991.

Wang, Z., W. P. Harbert, R. M. Dilmore, and L. Huang, 2018, Modeling of time-lapse seismic monitoring using CO_2 leakage simulations for a model CO_2 storage site with realistic geology: Application in assessment of early leak-detection capabilities: International Journal of Greenhouse Gas Control, **76**, 39–52, doi: 10.1016/j.ijggc.2018.06.011.

White, D. J., L. A. N. Roach, and B. Roberts, 2015, Time-lapse seismic performance of a sparse permanent array: Experience from the Aquistore CO_2 storage site: GEOPHYSICS, **80**, no. 2, WA35–WA48, doi: 10.1190/geo2014-0239.1.

White, J. C., G. A. Williams, and R. A. Chadwick, 2013, Thin layer detectability in a growing CO_2 plume: Testing the limits of time-lapse seismic resolution: Energy Procedia, **37**, 4356–4365, doi: 10.1016/j.egypro.2013.06.338.

Widess, M. B., 1973, How thin is a thin bed?: GEOPHYSICS, **38**, 1176–1180, doi: 10.1190/1.1440403.

Williams, G. A., and R. A. Chadwick, 2012, Quantitative seismic analysis of a thin layer of CO_2 in the Sleipner injection plume: GEOPHYSICS, **77**, no. 6, R245–R256, doi: 10.1190/geo2011-0449.1.

Wood, A. B., 1955, A textbook of sound, 3rd revised ed.: G. Bell and Sons.

Supplementary material

Figures S1–S10 support the paper above and are numbered in the order the text first cites them.

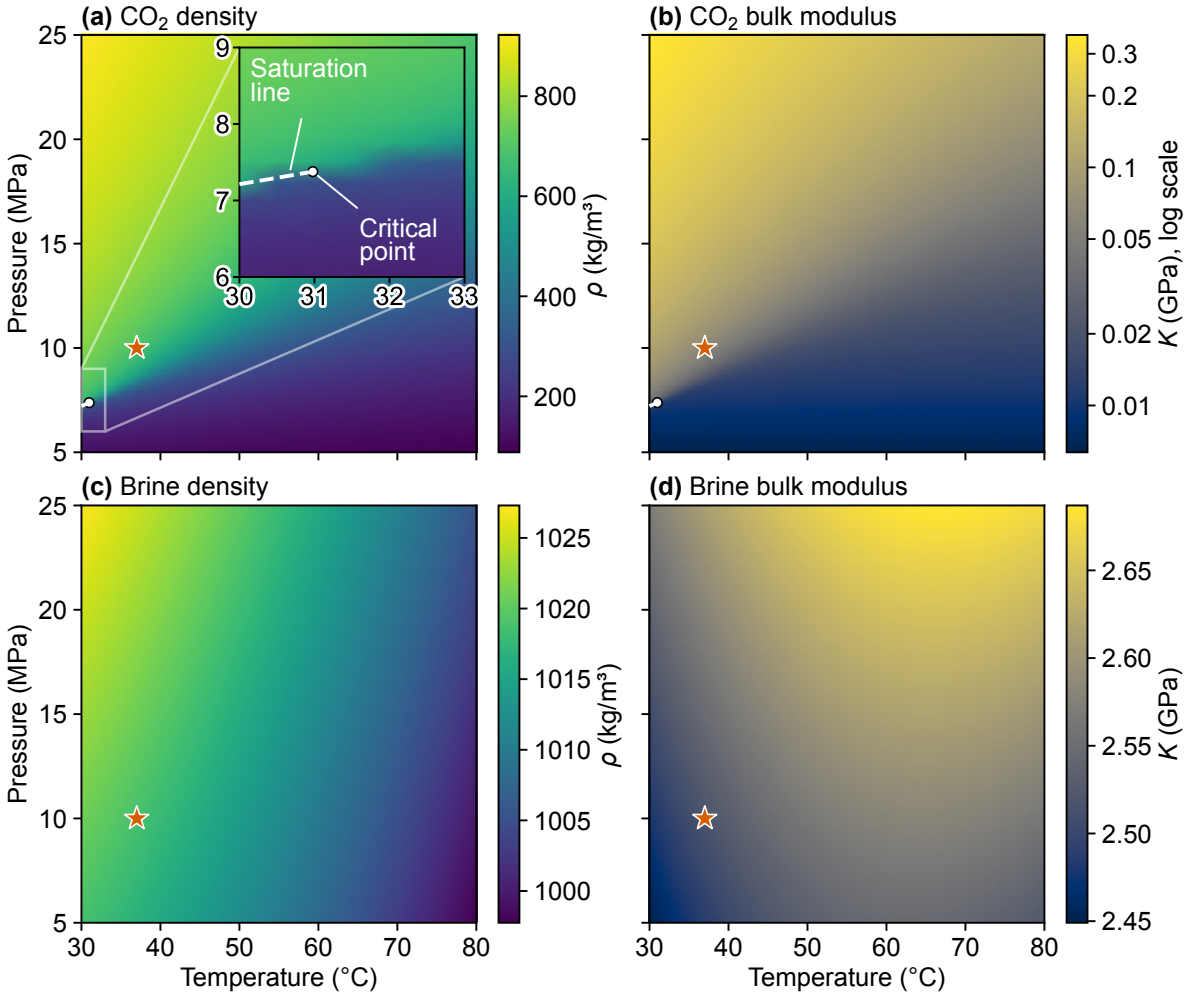


Figure S1. Fluid properties over the 41 × 51 pressure-temperature grid: (a) CO_2 density, with an inset showing the saturation line and the critical point; (b) CO_2 bulk modulus, on a logarithmic color scale; (c) brine density; (d) brine bulk modulus. Stars mark the reference condition, 37 °C and 10 MPa, used in every detection run.

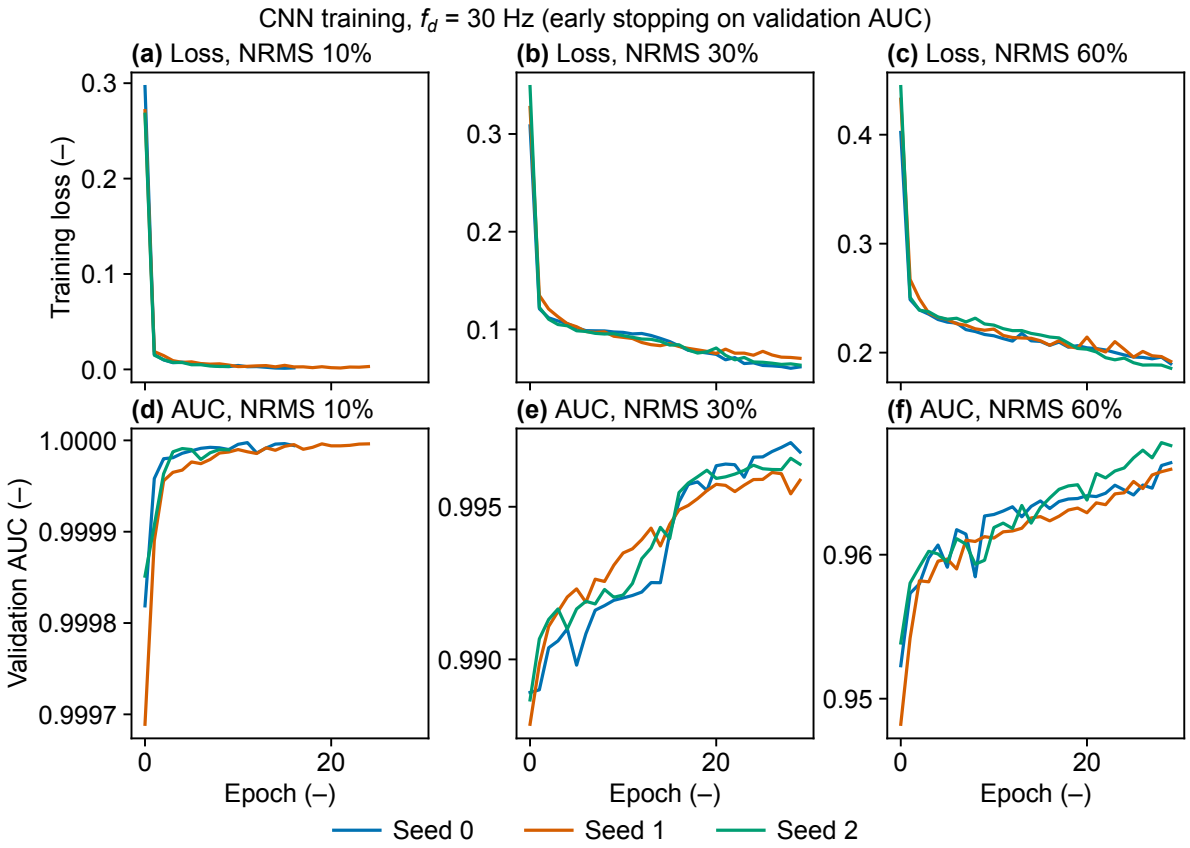


Figure S2. CNN training at 30 Hz for NRMS 10%, 30%, and 60% (columns): (a–c) training loss and (d–f) validation AUC versus epoch for each of the 3 training seeds. Training stops after 5 epochs without improvement in validation AUC; at NRMS 30% and 60% every seed ran the full 30 epochs.

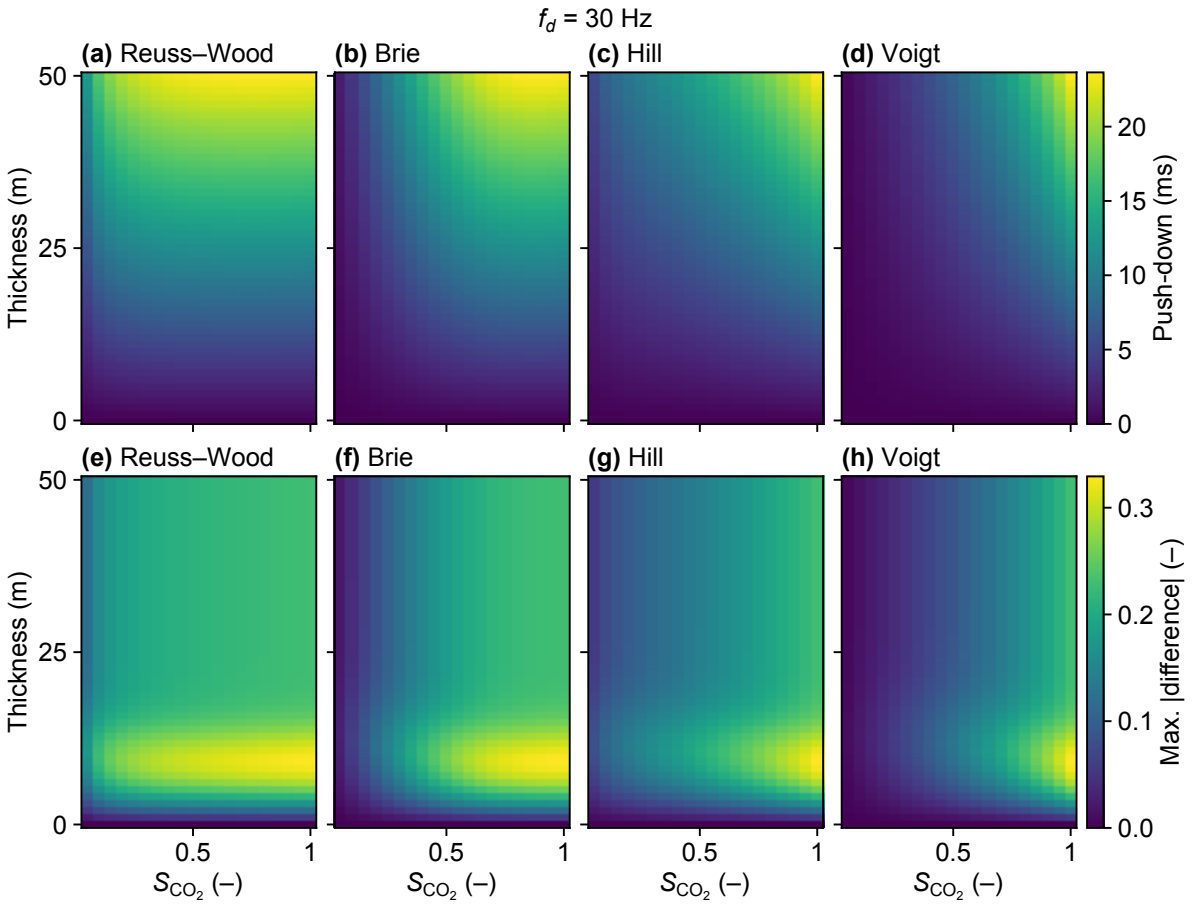


Figure S3. 4D attributes of the 1D layer models at 30 Hz over CO_2 layer thickness and saturation for the four mixing treatments (columns: Reuss–Wood, Brie, Hill, and Voigt): (a–d) push-down of the deep reflection and (e–h) maximum absolute difference amplitude in the layer window.

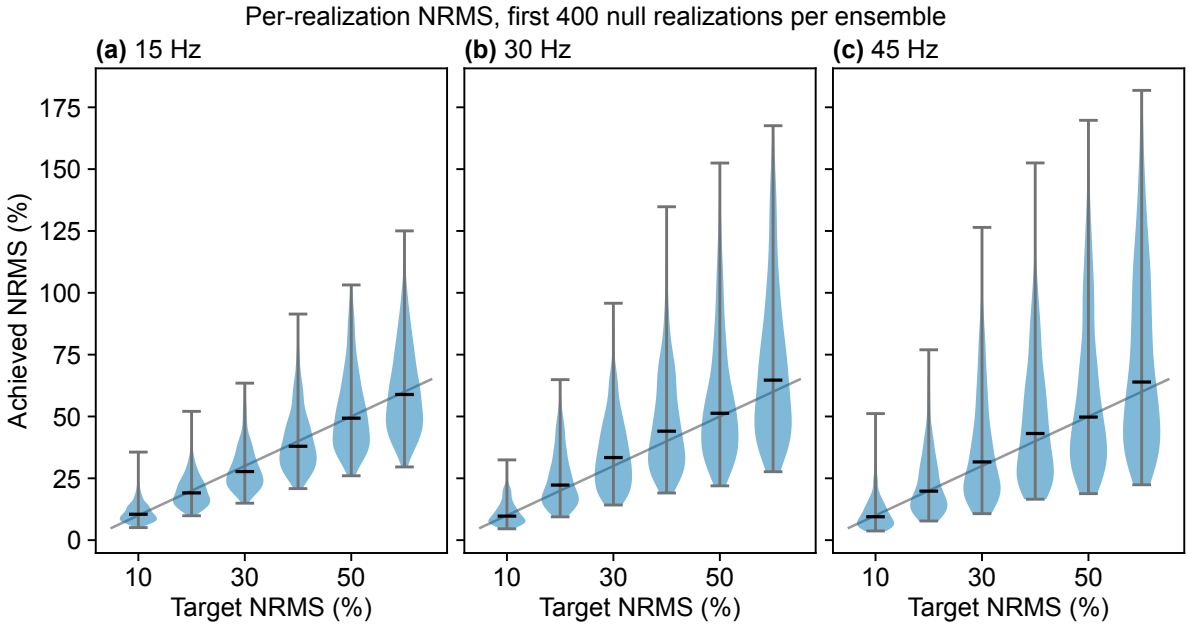


Figure S4. Achieved NRMS of single null realizations against the target NRMS at (a) 15, (b) 30, and (c) 45 Hz, measured in a window centered on the deep reflection. Violins show the distribution over the first null realizations drawn in each ensemble (the count is given above the panels), black bars the medians, gray whiskers the full range, and the gray line equality of achieved and target NRMS.

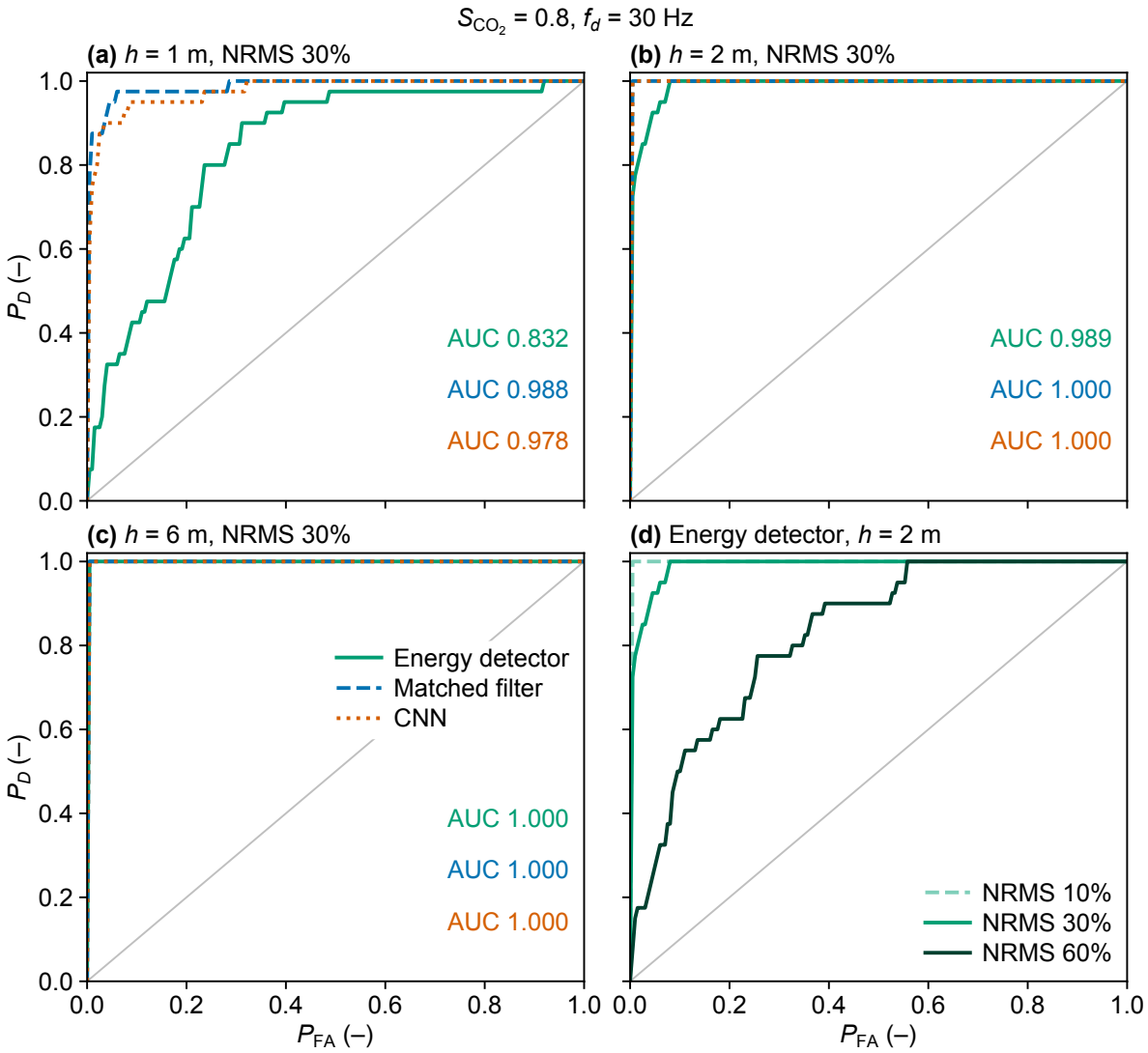


Figure S5. Receiver operating characteristic curves at 30 Hz and S_{CO_2} = 0.8: (a–c) energy detector, matched filter, and CNN at NRMS 30% for h = 1, 2, and 6 m, with the AUC of each detector; (d) the energy detector at h = 2 m for NRMS 10%, 30%, and 60%. The gray diagonal is chance performance. The CNN curves come from one training seed (seed 0), retrained for this figure and evaluated on the held-out test realizations; training on the GPU is not bit-for-bit repeatable, so these CNN AUC values can differ slightly from those of the stored seed-0 network.

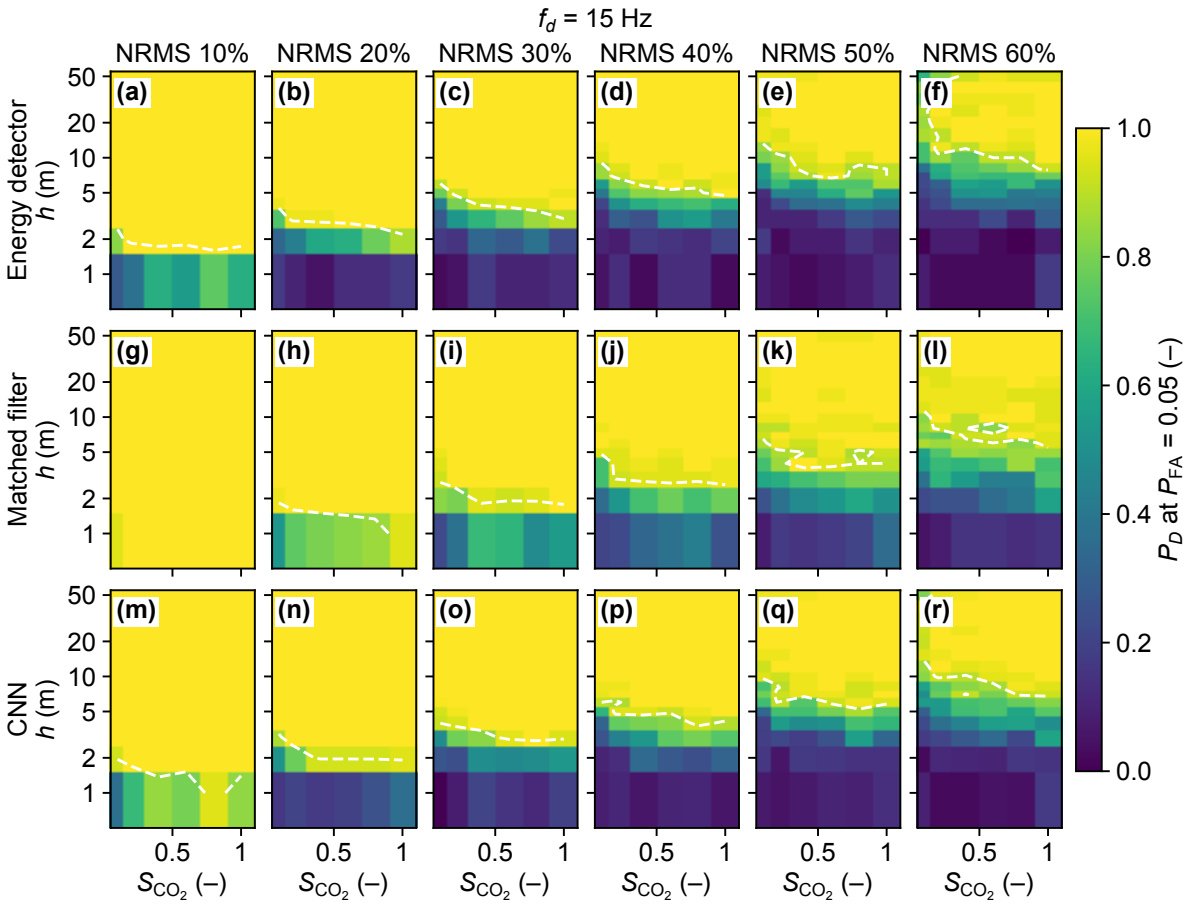


Figure S6. Detection probability at $P_{FA} = 0.05$ over thickness and saturation at 15 Hz for the (a–f) energy detector, (g–l) matched filter, and (m–r) CNN at six NRMS levels; dashed contours mark $P_D = 0.9$; CNN values are means over 3 seeds. The main text shows the same maps at 30 Hz.

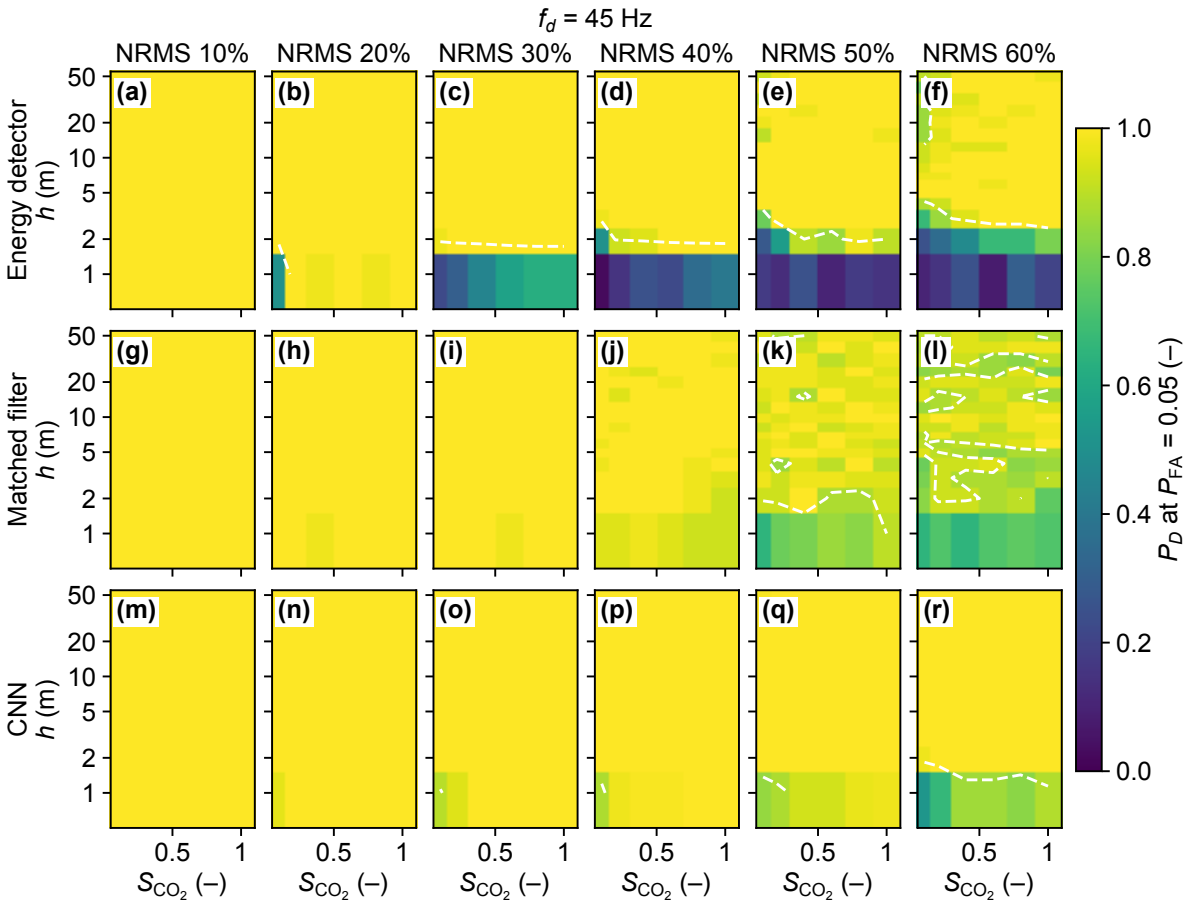


Figure S7. Detection probability at $P_{\mathrm{FA}} = 0.05$ over thickness and saturation at 45 Hz for the (a–f) energy detector, (g–l) matched filter, and (m–r) CNN at six NRMS levels; dashed contours mark $P_D = 0.9$; CNN values are means over 3 seeds. The main text shows the same maps at 30 Hz.

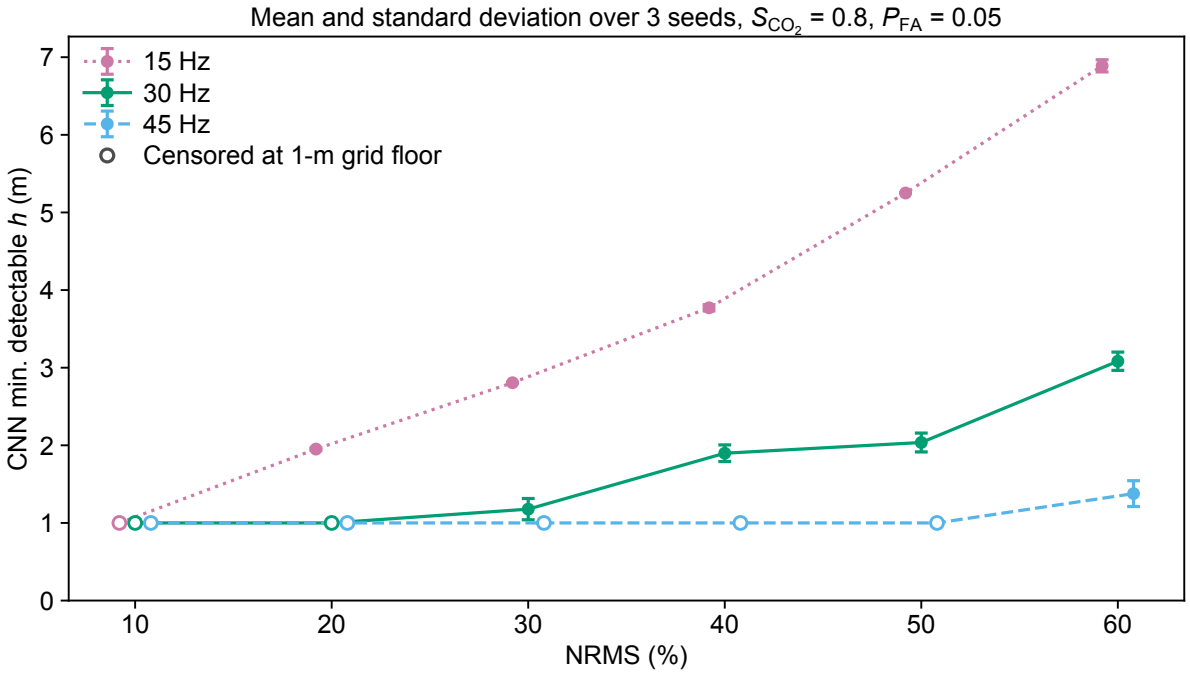


Figure S8. CNN minimum detectable thickness versus NRMS at 15, 30, and 45 Hz (S_{CO_2} = 0.8, P_{FA} = 0.05): mean and standard deviation (error bars) over 3 training seeds; open markers are censored at the 1-m grid floor. Points at each NRMS level are offset horizontally for legibility.

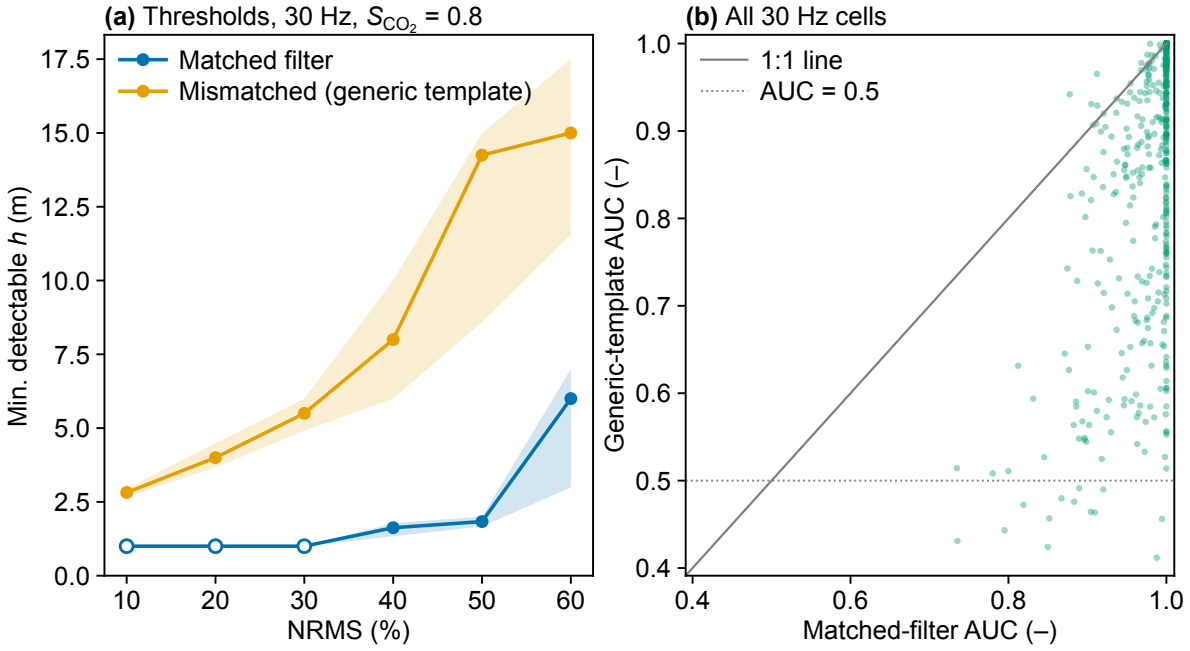


Figure S9. Clean-template matched filter against the generic-template filter at 30 Hz: (a) minimum detectable thickness versus NRMS at S_{CO_2} = 0.8, with bootstrap 10th–90th percentile bands and open markers for values censored at the 1-m grid floor; (b) generic-template AUC against matched-filter AUC for every 30-Hz cell, with the 1:1 line and the chance level.

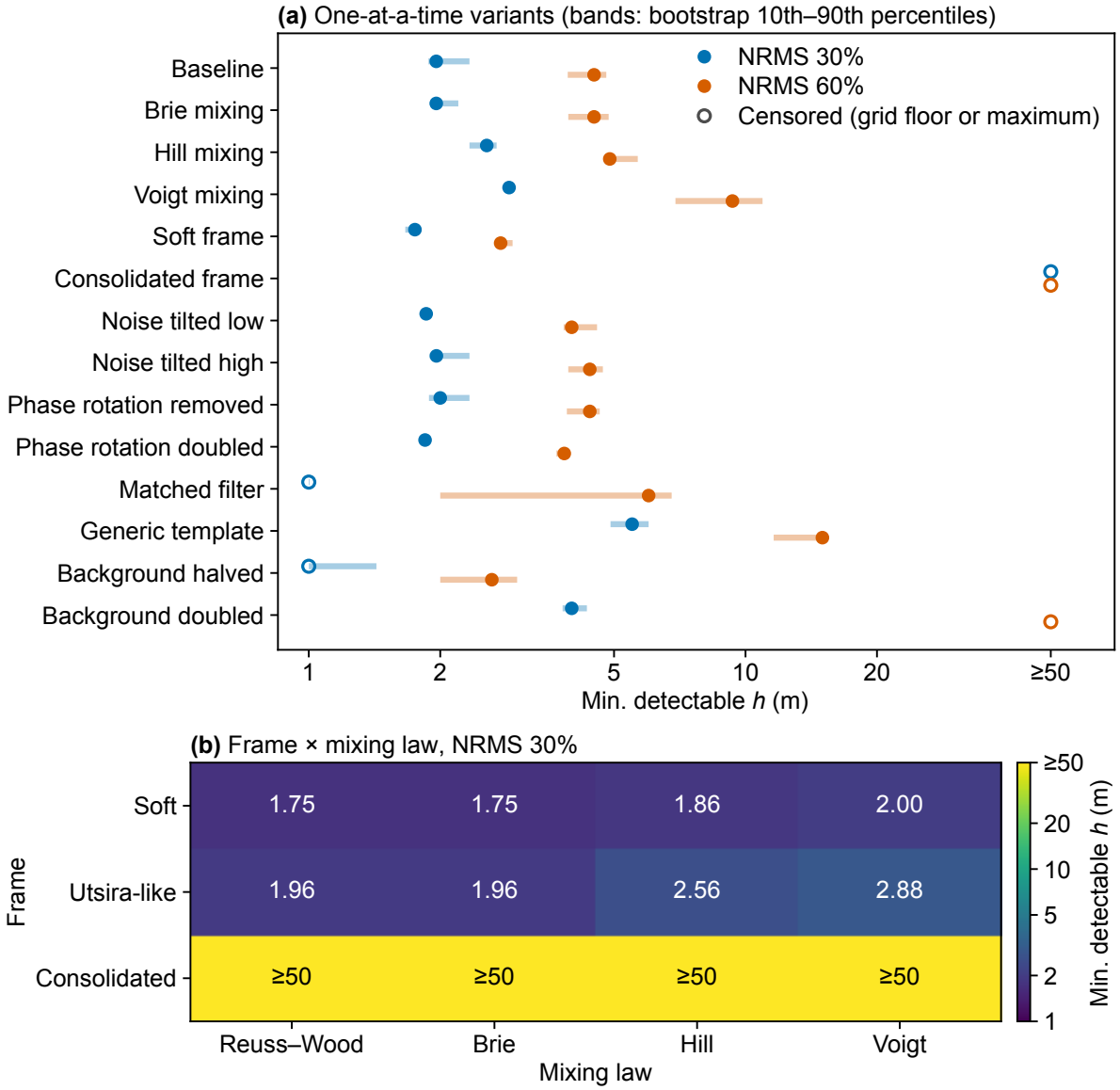


Figure S10. Sensitivity of the baseline threshold (energy detector, 30 Hz, $S_{CO_2} = 0.8$, $P_{FA} = 0.05$) to modeling assumptions: (a) minimum detectable thickness for each one-at-a-time variant, including the two detector swaps, at NRMS 30% and 60%, with 10th–90th percentile bands from the separate bootstrap of the sensitivity runs, which can differ slightly from the main-text bands, and open markers for values censored at the grid floor or beyond the 50-m grid maximum; (b) the frame-by-mixing-law factorial at NRMS 30%, in which the consolidated frame is censored beyond the grid maximum.